

Using diffusion MRI data acquired with ultra-high gradients to improve tractography in routine-quality data

C. Maffei^a, C. Lee^a, M. Planich^a, M. Ramprasada^a, N. Ravia^a, D. Trainora^a, Z. Urban^a, M. Kim^a, R.J. Jones^a, A. Henin^b, S.G. Hofmann^c, D.A. Pizzagalli^d, R.P. Auerbach^e, J.D.E. Gabrieli^f, S. Whitfield-Gabriel^g, D.N. Greve^a, S.N. Haber^{d,h}, A. Yendiki^a

^a Athinoula A. Martinos Center for Biomedical Imaging, Massachusetts General Hospital and Harvard Medical School, Charlestown, MA, USA

^b Massachusetts General Hospital and Harvard Medical School, Boston, MA, USA.

^c Boston University, Boston, MA, USA

^d McLean Hospital and Harvard Medical School, Belmont, MA, USA

^e Columbia University, New York, NY, USA

^f Massachusetts Institute of Technology, Cambridge, MA, USA

^g Northeastern University, Boston, MA, USA

^h Department of Pharmacology and Physiology, University of Rochester School of Medicine, Rochester, NY, USA

Corresponding author:

Chiara Maffei

cmaffei@mgh.harvard.edu

Athinoula A. Martinos Center for Biomedical Imaging

Massachusetts General Hospital and Harvard Medical School

149 Thirteenth Street | Charlestown | Massachusetts 02129

Abstract

The development of scanners with ultra-high gradients, spearheaded by the Human Connectome Project, has led to dramatic improvements in the spatial, angular, and diffusion resolution that is feasible for *in vivo* diffusion MRI acquisitions. The improved quality of the data can be exploited to achieve higher accuracy in the inference of both microstructural and macrostructural anatomy. However, such high-quality data can only be acquired on a handful of Connectom MRI scanners worldwide, while remaining prohibitive in clinical settings because of the constraints imposed by hardware and scanning time. In this study, we first update the classical protocols for tractography-based, manual annotation of major white-matter pathways, to adapt them to the much greater volume and variability of the streamlines that can be produced from today's state-of-the-art diffusion MRI data. We then use these protocols to annotate 42 major pathways manually in data from a Connectom scanner. Finally, we show that, when we use these manually annotated pathways as training data for global probabilistic tractography with anatomical neighborhood priors, we can perform highly accurate, automated reconstruction of the same pathways in much lower-quality, more widely available diffusion MRI data. The outcomes of this work include both a new, comprehensive atlas of WM pathways from Connectom data, and an updated version of our tractography toolbox, TRActs Constrained by UnderLying Anatomy (TRACULA), which is trained on data from this atlas. Both the atlas and TRACULA are distributed publicly as part of FreeSurfer. We present the first comprehensive comparison of TRACULA to the more conventional, multi-region-of-interest approach to automated tractography, and the first demonstration of training TRACULA on high-quality, Connectom data to benefit studies that use more modest acquisition protocols.

Keywords: Diffusion MRI; Tractography; White matter pathways; Neuroanatomy; Anatomical priors.

1 1. Introduction

2 Diffusion MRI (dMRI) tractography allows us to investigate the connectional anatomy of the
3 human brain *in vivo* and non-invasively. One of its applications is the delineation of white-
4 matter (WM) bundles that are known from the anatomical literature, with the goal of
5 studying their macro- and micro-structural properties in both healthy and clinical
6 populations.

7 Different methods have been proposed for extracting these bundles from whole-brain
8 tractograms. The majority of these methods follow the multi-region of interest (multi-ROI)
9 approach. Multi-ROI methods can be manual or automated. In the former case, ROIs are
10 hand-drawn in individual dMRI space by an operator (Catani and Thiebaut de Schotten 2008;
11 Wakana et al. 2007; Thiebaut de Schotten et al. 2011). For each WM bundle of interest, a set
12 of *a priori* rules define which ROIs the bundle does or does not go through. The rules are
13 applied to tractography streamlines obtained from each individual's dMRI data, and the ROIs
14 are refined manually to obtain bundles that match the anatomical literature as closely as
15 possible. This manual procedure is tailored to each individual subject, and therefore has the
16 potential to achieve high anatomical accuracy, to the extent that the initial streamlines
17 obtained from the subject's dMRI data are accurate. However, it is time-intensive and
18 requires extensive prior anatomical knowledge on the part of the operator, limiting
19 reproducibility and applicability to large datasets (Rheault et al. 2020). Automated multi-
20 ROI methods follow a similar approach, but derive the ROIs either from atlases (Clayden et
21 al. 2009; Yeatman et al. 2012; Groot et al. 2013; W. Zhang et al. 2008) or from automated,
22 subject-specific, anatomical segmentations (Wassermann et al. 2013). This is faster than the
23 manual approach and not operator-dependent. However, methods that rely on accurate
24 registration of each individual to an atlas may be sensitive to individual anatomical
25 variability. Importantly, both manual and automated multi-ROI methods are applied to
26 tractography streamlines as a post-processing step. As a result, their accuracy is intrinsically
27 limited by the quality of those streamlines, and therefore by the quality of the individual
28 dMRI data. An alternative family of bundle segmentation methods relies on clustering
29 algorithms, which group whole-brain tractography streamlines into clusters based on their

30 similarity (O'Donnell et al. 2007; Visser et al. 2011; Garyfallidis et al. 2012; Ros et al. 2013;
31 Siless et al. 2018). Each cluster of streamlines can then be labeled as a specific WM bundle,
32 either based on its similarity to manually labeled bundles, or based on multi-ROI rules
33 (Wasserman et al. 2010; Guevara et al. 2012; Garyfallidis et al. 2018; F. Zhang et al. 2018).

34 All of the above methods perform *post hoc* classification of tractography streamlines. If a
35 subject's tractogram does not contain any streamlines from a certain WM bundle, these
36 methods will not be able to recover this bundle. Previous studies have shown that the
37 precision and reliability of tractography are largely influenced by image quality and hence
38 by the acquisition protocol (Jbabdi and Johansen-Berg 2011; Vos et al. 2012; Calabrese et al.
39 2014; C. Maffei, Sarubbo, and Jovicich 2019). The technical advances spearheaded by the
40 Human Connectome Project (HCP) led to MRI systems with ultra-high gradients, which can
41 achieve high diffusion weighting (b-value) without loss of signal-to-noise ratio, as well as
42 accelerated MRI sequences that enable high angular and spatial resolution (Setsompop et al.
43 2013). However, dMRI data acquired in clinical settings typically have much lower quality,
44 due to MRI hardware limitations and scan time constraints. This limits the accuracy of
45 tractography, especially in bundles that are challenging because of their anatomical location,
46 size or shape. The multi-ROI methods described above cannot address this. Even if the ROIs
47 are defined on an atlas obtained from high-quality data, they cannot improve the
48 reconstruction of WM bundles in individual data collected with poorer signal-to-noise ratio,
49 spatial or angular resolution.

50 In this study we demonstrate how WM bundles labeled manually in high-quality data can be
51 used to ensure accurate, automated reconstruction of the same bundles in routine-quality
52 data. First, we describe a protocol for the manual dissection of 42 WM bundles from high-
53 quality, high-b data collected on a Connectom scanner by the HCP. These data allow us to
54 generate a much more detailed and accurate definition of the major bundles of the human
55 brain than what would be possible from routine-quality data. Our virtual dissection
56 protocols are more detailed than previously proposed ones (Wakana et al. 2007), to handle
57 the much greater volume and variability of the streamlines produced by today's state-of-the-
58 art data acquisition, orientation modeling, and tractography methods.

59 Second, we use these manually dissected WM bundles as a new training dataset for TRACULA
60 (TRActs Constrained by UnderLying Anatomy) (Yendiki et al. 2011). In contrast to multi-ROI
61 or clustering-based methods for bundle reconstruction, TRACULA does not operate on
62 tractography streamlines as a post-processing step. Instead, it incorporates prior
63 information on WM anatomy in the tractography step itself. This is done via a Bayesian
64 framework for global tractography that incorporates prior probabilities on the anatomical
65 neighborhood of WM bundles. Here we demonstrate that, when these prior probabilities are
66 computed from high-quality training data, TRACULA can reconstruct the same bundles in
67 routine-quality data with high anatomical accuracy. Specifically, we train TRACULA on
68 bundles labeled manually from HCP data with a maximum b-value of $10,000\text{ s/mm}^2$, and use
69 it to reconstruct the same 42 bundles from data acquired with a b-value of $1,000\text{ s/mm}^2$. We
70 compare these reconstructions to those obtained by an automated multi-ROI approach. We
71 show that TRACULA achieves overall higher accuracy and reliability.

72 The contribution of this work is twofold: *(i)* an updated set of protocols for manual dissection
73 of 42 WM bundles that are appropriate for tractograms obtained from state-of-the-art
74 Connectom data and *(ii)* a demonstration of automated tractography that can achieve a form
75 of “quality transfer” from Connectom data to more routine, clinical-quality data. Both the
76 manually labeled tracts, and the refactored version of TRACULA that uses them as training
77 data, are included in FreeSurfer 7.2 (<https://github.com/freesurfer/freesurfer/tree/fs-7.2-beta>). Extensive documentation and tutorials are available on the FreeSurfer wiki
78 (<https://surfer.nmr.mgh.harvard.edu/fswiki/Tracula>). Visualizations of the 42 manually
79 annotated WM bundles, as well as along-tract profiles of microstructural measures on these
80 bundles, are available at: <https://dmri.mgh.harvard.edu/tract-atlas/>.

82 **2. Methods**

83 **2.1 Overview**

84 We used state-of-the-art tractography techniques on the $b_{\max}=10,000\text{ s/mm}^2$ HCP data to
85 produce high-quality, whole-brain tractograms. We applied a manual, multi-ROI approach to
86 delineate a set of 42 WM bundles from these tractograms. We then used the manually
87 annotations to inform two methods (TRACULA and multi-ROI) for reconstructing the same

88 bundles automatically from the $b=1,000\text{ s/mm}^2$ data of the same subjects. We quantified the
89 accuracy of each method by computing the distance of the bundles that were reconstructed
90 automatically on the $b=1,000\text{ s/mm}^2$ data from those that were annotated manually on the
91 $b_{\max}=10,000\text{ s/mm}^2$ data of the same subject. We also assessed the test-retest reliability of
92 along-tract microstructural measures obtained from the automatically reconstructed
93 bundles, either with TRACULA or with the multi-ROI method. Finally, we used this updated
94 version of TRACULA to study associations between WM microstructure and
95 psychopathology in a larger, independent dataset.

96 **2.2 Data**

97 The manual annotation used diffusion and structural MRI data of 16 healthy adult subjects
98 provided by the MGH-USC HCP. The dMRI data include 512 diffusion-weighted (DW)
99 volumes (b -values= $1,000/3,000/5,000/10,000\text{ s/mm}^2$) and 40 non-DW volumes ($b=0$)
100 with 1.5 mm isotropic spatial resolution (Fan et al. 2015). The structural (T1-weighted) data
101 were acquired with a multi-echo magnetization-prepared rapid acquisition gradient echo
102 (MEMPRAGE) sequence at 1 mm isotropic resolution.

103 **2.3 Image analysis**

104 **2.3.1 Structural MRI**

105 Cortical parcellations and subcortical segmentations were obtained for each subject using
106 FreeSurfer (Dale, Fischl, and Sereno 1999; Fischl, Sereno, and Dale 1999, Fischl et al. 2002;
107 Fischl et al. 2004). Segmentations of the thalamic nuclei and hypothalamic subunits were
108 also obtained for each subject (Iglesias et al. 2015, 2018).

109 **2.3.2 Diffusion MRI.**

110 Diffusion data were denoised (Veraart et al. 2016) and corrected for gradient nonlinearity
111 distortions (Glasser et al., 2013; Jovicich et al., 2006). Data were then corrected for head
112 motion and eddy-current artifacts using *eddy* in FSL 6.0.3 (Andersson et al. 2016a, Andersson
113 et al. 2016b). For each subject, we obtained whole-brain probabilistic tractograms using two
114 methods: constrained spherical deconvolution (CSD) (Tax et al. 2014) on the $b = 10,000$
115 s/mm^2 shell only (step-size: 0.5 mm , angle-threshold: 30° , 10 seeds/voxel in white matter

116 mask) in DIPY (Garyfallidis et al. 2014) and multi-shell multi-tissue CSD (MSMT-CSD)
117 (Jeurissen et al. 2014) on all four shells (step-size: 0.75 mm, angle-threshold: 45°, 50
118 seeds/voxel in white matter mask) in MRtrix3 (Tournier et al. 2012). We used partial volume
119 masks of WM, gray matter (GM), and cerebrospinal fluid (CSF) to constrain the tractography
120 results (e.g., ensure that streamlines terminate at the GM-WM interface) (Smith et al. 2012).
121 We chose these two streamline tractography approaches empirically, after testing several
122 state-of-the-art, publicly available methods, as they yielded sharp orientation distribution
123 functions in fiber-crossing regions and in regions with partial voluming, respectively.

124 **2.4 Manual labeling in high-quality data**

125 We dissected 42 WM pathways manually in Trackvis (v.0.6.1; <http://www.trackvis.org>). For
126 each tract, we defined a combination of inclusion and exclusion ROIs in the space of each
127 individual subject. We derived protocols for the placement of these ROIs based on the
128 anatomical literature, as detailed in the following sections. Streamlines from an individual's
129 whole-brain tractogram (described in the previous section) were retained if they passed
130 through all inclusion ROIs and discarded if they passed through any of the exclusion ROIs
131 defined for a specific bundle. Any FreeSurfer cortical ROIs that were used for the manual
132 dissection came from the Desikan-Killiany parcellation (Desikan et al. 2006) and were grown
133 5 mm into the WM, along the normal vector of the cortical surface. The FreeSurfer corpus
134 callosum (CC) ROIs, wherever used, came from the subcortical segmentation and covered
135 only the section of the CC between the two hemispheres, along the midline. All projection
136 and association pathways were dissected in the left and right hemisphere, denoted in the
137 following as LH and RH, respectively. Each pathway was labeled by a single rater and then
138 checked by CM for correctness and consistency with neighboring pathways.

139 **2.4.1 Commissural pathways.**

140 The manual labeling protocol for these pathways is illustrated in Fig. 1.

141 *The Anterior Commissure (AC).* The AC was defined as a fiber bundle running transversely
142 between the anterior part of the bilateral temporal lobes and situated below the fornix
143 medially and the uncinate fascicle laterally (J. Schmahmann and Pandya 2006). We used
144 color-coded fractional anisotropy (FA) maps to draw a first inclusion ROI around the left-

145 right oriented region in front of the anterior columns of the fornix (sagittal view). Although
146 it has been suggested that the AC also includes posterior projections to the occipital lobe
147 (Turner, Mishkin, and Knapp 1979), we decided to include only the anterior limb of the AC
148 terminating in the WM of the temporal poles, as this is what is most commonly referred to
149 as the AC (Catani and Mesulam 2008; Lawes et al. 2008). Two more inclusion ROIs were thus
150 drawn to encompass the WM of the temporal pole in each hemisphere. A coronal ROI was
151 used to exclude the posterior projections, and two sagittal ROIs were used to exclude the
152 most lateral fibers of the AC adjacent to the external capsule.

153 *The Corpus Callosum (CC).*

154 *Genu:* The FreeSurfer segmentation label of the mid-anterior CC was used to select the
155 streamlines of the genu. A second and third ROI including medial and lateral regions of the
156 frontal lobe were used to include only frontal projections in both hemispheres and discard
157 spurious streamlines.

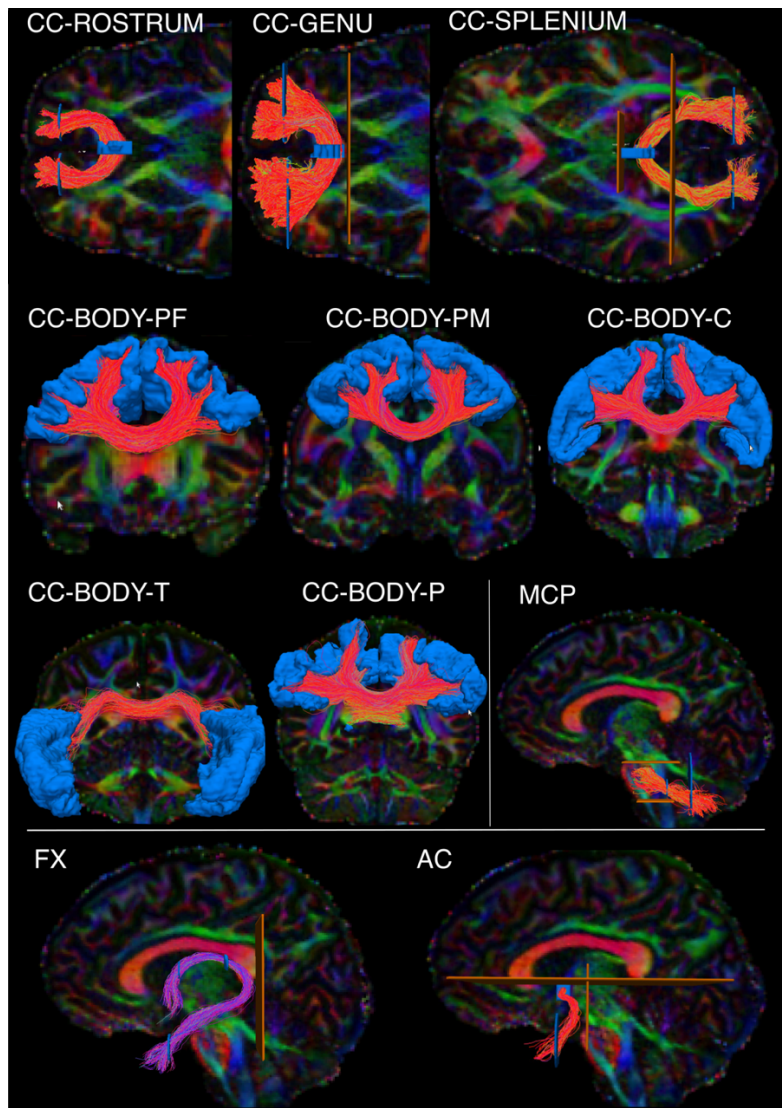
158 *Rostrum:* The FreeSurfer segmentation label of the anterior CC was used to select the
159 streamlines of the rostrum. A second and third ROI were used to include only streamlines
160 terminating in the orbital regions of the frontal cortex in each hemisphere.

161 *Splenium:* The splenium was defined as connecting parietal and occipital cortices.
162 Streamlines projecting to the temporal lobe were not included. The FreeSurfer regions of the
163 posterior and mid-posterior CC were used to select the streamlines of the splenium. A second
164 and third ROI encompassing the occipital and parietal WM were used to include only the
165 streamlines projecting posteriorly in each hemisphere.

166 *Body:* The inclusion ROIs of the genu, rostrum, and splenium in the frontal and occipital WM
167 were used as exclusion ROIs, to isolate the body of the CC from all other streamlines crossing
168 the FreeSurfer midline CC labels. Given the topographic organization of the CC, we further
169 subdivided the body into 5 sections, based on the cortical terminations of the streamlines.
170 The temporal section (BODY-T) included terminations in the FreeSurfer regions: superior
171 temporal, middle temporal, inferior temporal, transverse temporal, and banks of the
172 superior temporal sulcus. The parietal section (BODY-P) included terminations in regions:
173 superior parietal, supramarginal, and precuneus. The central section (BODY-C) included
174 terminations in regions: precentral, postcentral, and paracentral. Subdividing the remaining
175 (prefrontal and premotor) terminations of the body required subdividing the superior

176 frontal parcellation label, which is large and spans both of those termination areas. We used
177 a boundary from a previously proposed, publicly available parcellation scheme, which
178 translated anatomical definitions of cytoarchitectonic regions of the frontal cortex from
179 Petrides et al. 2012 to the fsaverage cortical surface (Tang et al. 2019). We mapped that
180 parcellation from the fsaverage surface to the individual surface of each training subject
181 using the inverse of the FreeSurfer spherical morph. We used the boundary that separated
182 areas 6, 8, and 44 from areas 9, 46, and 45 in that parcellation to subdivide the individual
183 superior frontal label from FreeSurfer into a caudal and a rostral parcel. We then defined a
184 premotor section of the body of the CC (BODY-PM) that included terminations in the caudal
185 subdivision of the superior frontal label or in the FreeSurfer caudal middle frontal label.
186 Finally, we defined a prefrontal section of the body of the CC (BODY-PF) that included
187 terminations in the rostral subdivision of the superior frontal label or in the FreeSurfer
188 rostral middle frontal label.

189 *The Fornix (FX).* The FX was defined as streamlines surrounding the thalamus, directly
190 adjacent to the medial half of its superior and posterior surfaces (Pascalau et al. 2018) and
191 connecting the hippocampal formation (specifically CA1, CA3, and fimbria) with the anterior
192 thalamic nuclei, the mammillary bodies, the medial septal nucleus, and the basal forebrain
193 (Poletti and Creswell 1977; Christiansen et al. 2017). A first inclusion ROI was placed on the
194 coronal plane, inferior to the body of the CC, to outline the fornix body. A second inclusion
195 ROI was then placed inferior and lateral to the hippocampus, where the fornix terminates.
196 The subnuclei of the hippocampus (CA1, CA3, fimbria) (Iglesias et al. 2015) were used to
197 confirm the correct terminations of the fornix. The tract was refined by placing two more
198 inclusion ROIs anterior to the splenium of CC on a coronal slice to encompass each respective
199 crus of the fornix. One exclusion ROI was then placed posterior to the crus to discard
200 spurious streamlines.



201

202 **Fig. 1. Manual labeling: commissural pathways.** The figure shows the manual labeling protocols for
203 the commissural pathways in one representative subject. Inclusion ROIs are shown in blue, exclusion
204 ROIs in orange. Tracts are shown on color-coded FA maps. CC: Corpus callosum. It is subdivided into the
205 rostrum, genu, splenium, and body. The body is further subdivided into prefrontal (BODY-PF), premotor
206 (BODY-PM), central (BODY-C), temporal (BODY-T), and parietal (BODY-P) components. MCP: middle
207 cerebellar peduncle. FX: fornix. AC: anterior commissure.

208 **2.4.2 Projection pathways**

209 The manual labeling protocol for these pathways is illustrated in Fig. 2.

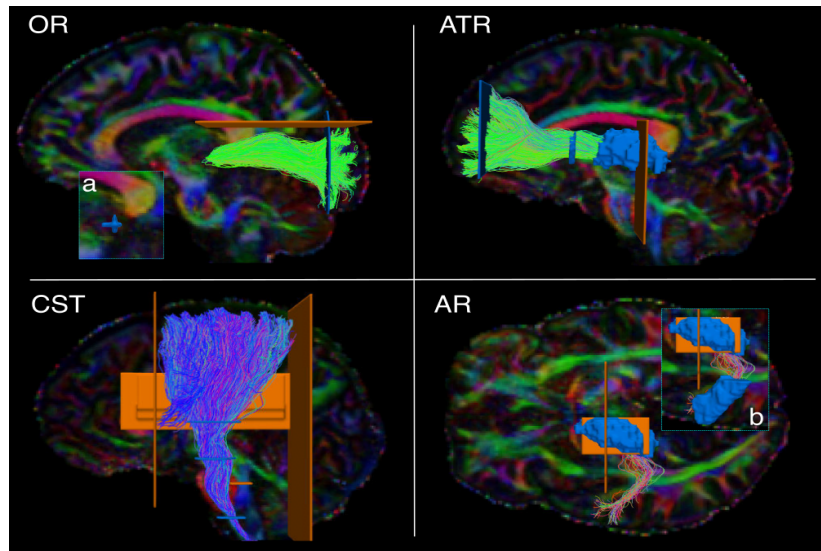
210 *The Acoustic Radiation (AR).* The AR was defined as fibers originating in posterior thalamus,
211 where the medial geniculate nucleus (MGN) is located, and terminating on the transverse

212 temporal gyrus of Heschl (HG) in the posterior portion of the superior temporal gyrus (STG)
213 (Bürgel et al. 2006; Rademacher, Bürgel, and Zilles 2002; Chiara Maffei et al. 2018). The
214 FreeSurfer segmentation label of the entire thalamus was used as a first inclusion ROI, and a
215 second inclusion ROI was manually drawn to encompass the GM and WM of the HG as
216 previously described (C. Maffei, Sarubbo, and Jovicich 2019).

217 *The Anterior Thalamic Radiation (ATR).* The ATR was defined as fibers originating in the
218 anterior and medial thalamus, passing through the anterior limb of the internal capsule
219 (ALIC), and connecting to the prefrontal cortex (Wakana et al. 2007). The Freesurfer
220 segmentation label of the entire thalamus was used as the first inclusion ROI. A second
221 inclusion ROI was drawn on a coronal slice to encompass the prefrontal WM of the superior
222 and middle frontal gyrus. A third inclusion ROI was drawn on the ALIC on a coronal slice. An
223 exclusion ROI was placed on the midline (sagittal plane) to remove streamlines crossing to
224 the contralateral hemisphere through the CC.

225 *The Cortico-Spinal Tract (CST).* The CST was defined as streamlines passing through the
226 midbrain, the medulla oblongata, and the internal capsule (first, second, third inclusion ROI,
227 respectively). We retained its terminations in the precentral and postcentral gyri, as well as
228 the posterior third of the superior frontal gyrus, corresponding to the supplementary motor
229 area (SMA) (Chenot et al. 2019). Two coronal exclusion ROIs were placed to discard
230 streamlines projecting too anteriorly or posteriorly: one posterior to the postcentral sulcus,
231 and one anterior to the SMA. Additional exclusion ROIs were drawn on the midline (sagittal
232 plane) and the tegmental tract (axial plane).

233 *The Optic Radiation (OR).* The OR was defined as connecting the thalamus and the occipital
234 cortex (Kammen et al. 2016; Sarubbo et al. 2015). The whole thalamus as segmented in
235 FreeSurfer was used as a first inclusion ROI. A second inclusion ROI (coronal plane) was used
236 to encompass the WM of the occipital lobe. An exclusion ROI (coronal plane) was used to
237 discard the posterior projections of the CC. Another exclusion ROI was drawn on the axial
238 plane to discard streamlines projecting too superiorly.



239

240 **Fig. 2. Manual labeling: projection pathways.** The figure shows the manual labeling protocols for the
241 projection pathways in one representative subject. Inclusion ROIs are shown in blue, exclusion ROIs in
242 orange. Tracts are shown on color-coded FA maps. OR: optic radiation. ATR: anterior thalamic
243 radiation. CST: cortico-spinal tract. AR: acoustic radiation. a) zoom-in showing ROI on the lateral
244 geniculate nucleus of the thalamus. b) zoom-in showing ROI on Heschl's gyrus.

245 **2.4.3 Association pathways**

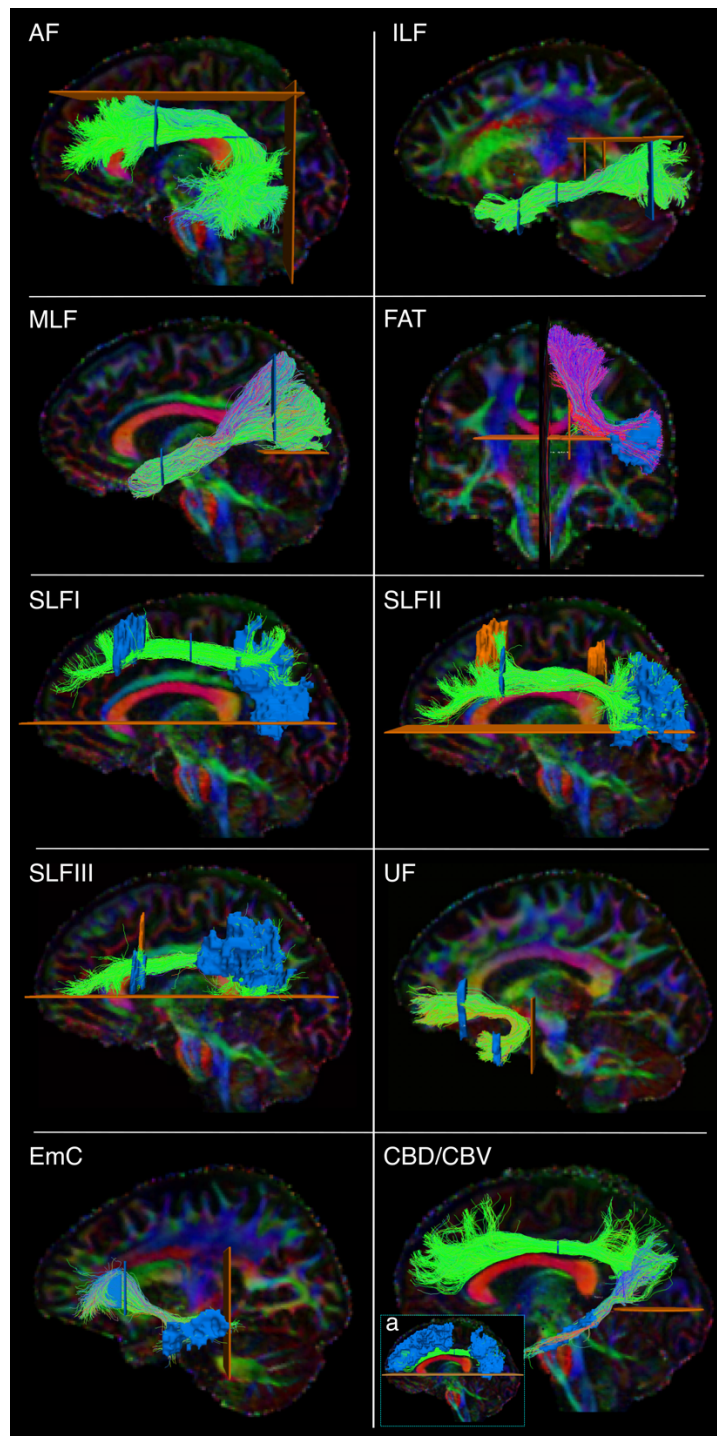
246 The manual labeling protocol for these pathways is illustrated in Fig. 3.

247 *The Arcuate Fasciculus (AF).* The AF was defined as the long, direct connections arching
248 around the Sylvian fissure and connecting temporal (inferior, middle, and superior temporal
249 gyri) and frontal regions (Catani, Jones, and Ffytche 2005; Lawes et al. 2008; J. D.
250 Schmahmann et al. 2007; Makris et al. 2005; Fernández-Miranda et al. 2015). A first inclusion
251 ROI was drawn on 3 consecutive axial slices at the level of the main body of the CC (medial
252 boundary: line between arcuate and corona radiata; lateral boundary: postcentral sulcus;
253 anterior boundary: precentral sulcus; posterior boundary: intraparietal sulcus). A second
254 inclusion ROI was placed on a coronal slice at the level of the precentral sulcus (medial
255 boundary: lateral ventricle; lateral/ventral/dorsal boundary: GM around Sylvian fissure and
256 parietal lobe sulci) (Catani and Mesulam 2008). One exclusion ROI was drawn on a sagittal
257 slice just lateral to the corona radiata, to remove erroneously crossing streamlines to the
258 contralateral hemisphere. Two additional exclusion ROIs were placed superior and posterior
259 to the AF to remove spurious streamlines.

260 *The Cingulum Bundle (CB).* The CB was defined as a long associative bundle running in the
261 WM adjacent to the cingulate gyrus (CG), arching around the splenium of the CC at the level
262 of the cingulate isthmus, and terminating at the parahippocampal gyrus (J. Schmahmann and
263 Pandya 2006; Lawes et al. 2008). To isolate the CB streamlines, a first ROI was drawn to
264 include the anterior-posterior oriented regions superior to the CC as identified on coronal
265 color-coded FA maps. We then subdivided the CB in two sub-bundles (Wakana et al. 2007;
266 Jones, Knösche, and Turner 2013): a dorsal component running in the CG (CBD) and a ventral
267 component running in the parahippocampal gyrus (CBV). We defined the CBD as connecting
268 the anterior CG and the superior frontal gyrus (SFG) with parietal WM superior to the
269 splenium of the CC, and the CBV as connecting these superior regions with the
270 parahippocampal gyrus. One exclusion ROI was placed on one axial slice inferior to the
271 splenium of the CC to exclude ventral streamlines from the CBD (Fig. 3a), and one on one
272 axial slice inferior and posterior to the splenium of the CC for the CBV.

273 *The Extreme Capsule (EmC).* The EmC was defined as streamlines connecting the frontal and
274 temporal regions, and located lateral to the uncinate fasciculus (UF) (Heide et al 2013). A
275 first hand-drawn inclusion ROI was placed in the SFG to encompass most of the WM
276 Brodmann's areas 9 and 10 (Mars et al. 2016; Makris et al. 2009). This ROI was placed on the
277 sagittal plane to make sure to distinguish EmC streamlines projecting laterally from UF
278 streamlines projecting anteriorly (see below for UF dissection protocol). A second hand-
279 drawn inclusion ROI was placed in the MTG. An exclusion ROI was located on the coronal
280 plane posterior to the STG. A large exclusion ROI was placed along the midline of the brain.

281 *The Frontal Aslant Tract (FAT).* The FAT was defined as streamlines connecting the posterior
282 inferior frontal gyrus (IFG), pars opercularis, and medial aspects of the SFG, namely the pre-
283 SMA and SMA (J. Schmahmann and Pandya 2006; Dick et al. 2019; Lawes et al. 2008).
284 Exclusion ROIs were placed on a coronal slice posterior to the SMA and anterior to the pre-
285 SMA, on the sagittal plane to exclude streamlines entering the CC, and on the axial plane to
286 exclude artefactual streamlines projecting inferior.



287

288 **Fig. 3. Manual labeling: association pathways.** The figure shows the manual labeling protocols for
289 the association pathways in one representative subject. Inclusion ROIs are shown in blue, exclusion ROIs
290 in orange. Tracts are shown on color-coded FA maps. AF: arcuate fasciculus. ILF: inferior longitudinal
291 fasciculus. MLF: middle longitudinal fasciculus. FAT: frontal aslant tract. SLF: superior longitudinal
292 fasciculus. UF: uncinate fasciculus. EmC: extreme capsule. CBD/CBV: dorsal and ventral part of the
293 cingulum bundle. a) inclusion and exclusion ROIs for the CBD.

294 *The Inferior Longitudinal Fasciculus (ILF)*. The ILF was defined as streamlines connecting
295 superior, middle, inferior occipital gyri, and the fusiform and lingual gyri to the inferior and
296 middle temporal gyri and the temporal pole (Latini et al. 2017). A first inclusion ROI was
297 placed on a coronal slice, at the level of the precentral sulcus, to outline the temporal lobe,
298 excluding the superior temporal sulcus. A second inclusion ROI was placed posterior to the
299 CBD on a coronal slice to encompass the occipital WM. One exclusion ROI was placed
300 superiorly (axial plane) to discard parietal connections, and one medially to the ILF (sagittal
301 plane) to discard spurious streamlines.

302 *The Middle Longitudinal Fasciculus (MLF)*. The MLF was defined as streamlines connecting
303 the superior and middle anterior temporal gyri and the temporal pole with the superior and
304 inferior parietal cortex, coursing medial to the AF and superior to the ILF (Menjot De
305 Champfleur et al. 2013; N. Makris et al. 2013; J. Schmahmann and Pandya 2006; Maldonado
306 et al. 2013). A first inclusion ROI was placed on a coronal slice at the level of the precentral
307 sulcus, to outline the superior temporal lobe. A second inclusion ROI was placed posterior to
308 the CBD on a coronal slice to include both the superior and inferior parietal WM. An exclusion
309 ROI was placed on the axial plane at the level of the parieto-occipital sulcus to discard
310 streamlines going into the occipital lobe.

311 *The Superior Longitudinal Fasciculus (SLF)*. We dissected three SLF branches following
312 definitions from the anatomical literature (J. D. Schmahmann et al. 2007; Hecht et al. 2015;
313 Howells et al. 2018). SLF1: We placed one inclusion ROI in the superior frontal gyrus and one
314 encompassing the WM posterior to the posterior central gyrus and dorsal to the cingulate
315 sulcus. SLF2: We placed one inclusion ROI in the caudal part of the middle frontal gyrus and
316 one in the WM of the inferior parietal lobe (Thiebaut de Schotten et al. 2011; Makris et al.
317 2009). SLF3: We placed one inclusion ROI in the posterior inferior frontal gyrus and one in
318 the anterior supramarginal gyrus (J. D. Schmahmann et al. 2007; Hecht et al. 2015; Howells
319 et al. 2018). For all three bundles, we used mid-sagittal and temporal exclusion ROIs.

320 *The Uncinate Fasciculus (UF)*. The UF was defined as streamlines connecting the anterior
321 temporal pole and anterior middle temporal gyrus (MTG) with the medial and orbital
322 prefrontal cortex (J. Schmahmann and Pandya 2006; Catani and Mesulam 2008). These
323 streamlines were identified as medial and inferior to the EmC. The first inclusion ROI was

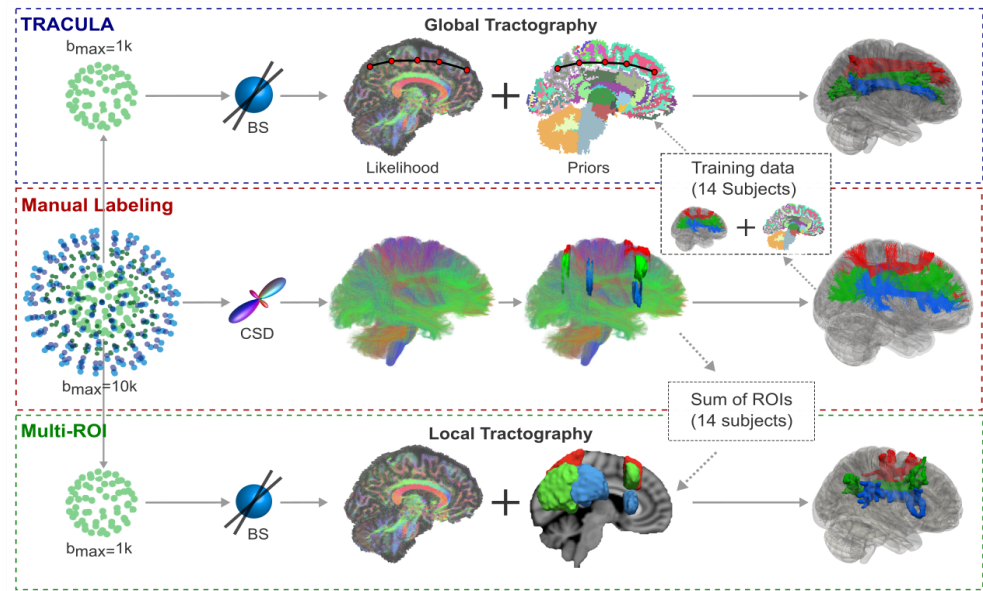
324 drawn on four consecutive coronal slices in the temporal lobe, to encompass the WM of the
325 MTG and temporal pole. A second inclusion ROI was drawn in the frontal lobe on four
326 consecutive coronal slices on the WM of the medial orbito-frontal cortex. The subgenual WM
327 was considered the upper limit of this ROI. Exclusion ROIs were placed on the mid-sagittal
328 slice between the two hemispheres and directly posterior to the stem of the UF to exclude
329 erroneous streamlines. We ensured that the relative position of the UF with respect to the
330 EmC was accurate in each subject by labeling these two tracts jointly.

331 **2.5 Automated reconstruction in routine-quality data**

332 The bundles that were labeled manually in the $b_{\max} = 10,000 \text{ s/mm}^2$ data, were also
333 reconstructed automatically in the $b=1000 \text{ s/mm}^2$ data of the same subjects (Fig. 4). The
334 $b=1000 \text{ s/mm}^2$ shell comprised 64 out of the 512 DW volumes. We compared two
335 approaches to automated reconstruction: (i) TRACULA, where we used the manually labeled
336 bundles from the $b_{\max} = 10,000 \text{ s/mm}^2$ data to compute prior probabilities on the anatomical
337 neighborhood of each bundle and incorporated them in a Bayesian framework global
338 probabilistic tractography, and (ii) Multi-ROI, where we used the group-averaged ROIs and
339 inclusion/exclusion rules from the manual labeling as post-hoc constraints for local
340 probabilistic tractography. We evaluated both approaches in a leave-one-out scheme, where
341 the automated reconstruction in each subject used the manually labeled bundles or the
342 labeling ROIs from the other 15 subjects.

343 **2.5.1 TRACULA**

344 *Training data:* The manual labeling procedure of section 2.4 produced a total of 2.29 million
345 streamlines over all 42 bundles and 16 training subjects, covering 82% of all cerebral and
346 cerebellar WM voxels. (In comparison, the manually labeled training set used in previous
347 versions of our software included a total of 0.15 million streamlines from 18 bundles, which
348 had been labeled in much lower-quality data and covered 18% of WM voxels.) This required
349 us to refactor the TRACULA code base extensively to be able to handle a much larger training
350 set than before. In this new, refactored version, many of the operations involved in
351 computing the anatomical neighborhood priors, which were previously computed on the fly,
352 are now precomputed and stored with the publicly distributed training data.



353

354 **Fig. 4. Overview of tractography methods.** From the four-shell MGH-USC HCP data, the
355 $b=10,000 \text{ s/mm}^2$ and $b=1000 \text{ s/mm}^2$ shells were extracted. Orientations were reconstructed with
356 constrained spherical deconvolution (CSD) from the $b=10,000 \text{ s/mm}^2$ shell and with multi-shell multi-
357 tissue CSD (MSMT-CSD) from all four shells. Streamline tractography was performed with these two
358 approaches and used to annotate 42 tracts manually in 16 subjects. The lower shell ($b=1000 \text{ s/mm}^2$,
359 64 directions) was used to reconstruct the same tracts automatically, with TRACULA or with a multi-
360 ROI approach. For TRACULA, anatomical priors for each subject were obtained from the other 15
361 subjects and global probabilistic tractography was performed. For the multi-ROI approach, inclusion
362 and exclusion masks were obtained from summing the manually defined ROIs of the other 15 subjects in
363 template space. Local probabilistic tractography was constrained by these ROIs. The same ball-and-
364 stick (BS) diffusion model was used for both TRACULA and the multi-ROI approach.

365 In addition, the densest of the manually labeled bundles, e.g., most subdivisions of the CC,
366 included a large number of streamlines with very similar anatomical neighbors. As a result,
367 we could use a subset of these streamlines without affecting the computation of the
368 anatomical priors. Therefore, for any WM bundle that included more than 20,000 training
369 streamlines, we reduced that number to 20,000 to speed up this computation. We first
370 removed outlier streamlines, which can be difficult to remove manually one by one,
371 particularly for very dense bundles. Outliers were detected by mapping the end points of the
372 streamlines to a common template space (see below for more information on registration),
373 summing the endpoints over all subjects, and clustering them. Small clusters of endpoints

374 were tagged as outliers and any individual streamlines that terminated in those outlier
375 clusters were removed. If the total number of streamlines in a bundle was still above 20,000,
376 it was reduced further by random subsampling of the streamlines. Note that this reduced set
377 of streamlines was used to train TRACULA, but the complete set of 2.29 million streamlines
378 was used as the “ground truth” to evaluate the accuracy of the automated reconstruction.

379 *Anatomical neighborhood priors:* For each subject, we used the 42 manually defined bundles
380 from each of the other 15 subjects as the training set. The mathematical formulation has been
381 described elsewhere (Yendiki et al. 2011; Yendiki et al. 2016). Briefly, this approach models
382 a WM pathway as a cubic spline, which is initialized with the median streamline of the
383 training set. A random sampling algorithm is used to draw samples from the posterior
384 probability distribution of the pathway by perturbing the control points of the spline. The
385 posterior probability is decomposed into the likelihood of the pathway given the DW
386 volumes and the prior probability of the pathway. The likelihood term fits the shape of the
387 spline to the diffusion orientations in the voxels that the spline goes through. As previously,
388 diffusion orientations were obtained by fitting the ball-and-stick model (Behrens et al. 2003)
389 to the subject’s DW volumes. This model does not require a sophisticated dMRI acquisition;
390 it can be used on data collected with low b-values and with as few as 30 directions (Behrens
391 et al. 2007).

392 The prior probability term in TRACULA fits the shape of a pathway to its anatomical
393 neighborhood, given the manually labeled examples of this pathway from the training
394 subjects and the anatomical segmentation volumes of both test and training subjects.
395 Specifically, the training streamlines are used to compute the prior probability that each
396 label of the anatomical segmentation is the j -th neighbor of the pathway at the i -th point
397 along the trajectory of the pathway. Here i indexes equispaced points (3 mm apart) along the
398 pathway and j indexes the nearest neighboring segmentation labels in different directions
399 (left, right, anterior, posterior, etc.) The anatomical labels were extracted from the subject’s
400 T1-weighted scan using FreeSurfer.

401 *Structural segmentation:* In this work, we used an anatomical segmentation volume that
402 combined the labels of the Desikan-Killiany cortical parcellation (Desikan et al. 2006) with
403 the standard FreeSurfer subcortical segmentation (Fischl et al. 2002). However, we replaced

404 the thalamus label of the latter with the subject's thalamic nuclei segmentation labels
405 (Iglesias et al. 2015, 2018). This replacement was done to avoid oversegmenting the
406 thalamus into WM voxels, and to provide additional specificity on the anatomical neighbors
407 of tracts that terminate in or travel around the thalamus. Computing the prior probabilities
408 on the anatomical neighbors of the tracts requires that each (training or test) subject's
409 anatomical segmentation be transformed to the subject's individual dMRI space. This within-
410 subject, dMRI-to-T1 alignment was performed by a boundary-based, affine registration
411 method (Greve and Fischl 2009).

412 *Template construction:* Although finding the anatomical neighbors of a tract is a within-
413 subject operation, it is important to ensure that all subjects' brains have the same
414 orientation, so that the relative positions of neighboring structures (which structure is to the
415 left/anterior/etc. of which tract) is equivalent for all subjects. For this purpose, and for
416 mapping the median of the training streamlines to the test subject during initialization,
417 subjects must be mapped onto a template brain. Here we constructed a template by co-
418 registering the FA maps of all 35 subjects in the MGH-USC HCP data set (Fan et al. 2015) with
419 symmetric normalization (SyN; Avants et al. 2008), as implemented in ANTs (Avants et al.
420 2011). An affine initial registration was followed by 4 iterations of nonlinear registration
421 with the b-spline SyN transform model, a cross-correlation similarity metric with a radius of
422 2, and a 4-level multi-resolution scheme with 100/70/50/50 sub-iterations per level. Each
423 test subject's FA map was aligned to the template with the default sequence of
424 rigid/affine/deformable SyN registration followed in ANTs. Although we are introducing this
425 nonlinear registration approach to TRACULA in the interest of generality, it is important to
426 note that the purpose for which TRACULA performs subject-to-template registration (to find
427 within-subject anatomical neighbors in a consistent set of directions) does not require exact
428 voxel-wise, inter-subject alignment. We demonstrate this here by comparing this nonlinear
429 registration approach to the one that was used by default in previous versions of TRACULA,
430 *i.e.*, affine registration of each subject's T1 image to the 1 mm MNI-152 template with FSL's
431 FLIRT (Jenkinson et al. 2002).

432 *Choice of control points:* The number of control points of the cubic spline, which are
433 perturbed at each iteration of the random sampling algorithm to draw new sample paths,
434 was chosen according to the average length of the training streamlines for each bundle.

435 Specifically, we chose the number of control points to be 5 for the genu of the CC, and we
436 then set the number of control points for all other bundles proportionally to their length.
437 This ranged from 4 control points for the ATR to 12 control points for the temporal
438 component of the body of the CC.

439 *Along-tract analysis:* Pointwise assessment of streamline tractography attributes (PASTA) is
440 a type of analysis where an along-tract profile of a microstructural measure (e.g., FA) is
441 generated by averaging the values of the measure at different cross-sections of a tract (Jones
442 et al. 2005). For each of the 42 bundles, we generated a reference streamline for PASTA
443 analyses, to ensure that all subjects are sampled at the same number of cross-sections along
444 a given bundle. The reference streamline was the mean of the manually annotated
445 streamlines in template space. After the bundles of an individual subject were reconstructed
446 automatically with TRACULA, the reference streamlines were mapped from the template to
447 the individual. We generated along-tract profiles of microstructural measures by projecting
448 the value of each measure from every point on every automatically reconstructed streamline
449 to its nearest point on the reference streamline. Values projected to the same point on the
450 reference streamline were then averaged, to generate an along-tract, 1D profile of the
451 microstructural measure.

452 **2.5.2 Multi-ROI**

453 For comparison, we also reconstructed each subject's bundles with a commonly used multi-
454 ROI approach, which maps a set of ROIs from a template to an individual subject's dMRI
455 space and combines them with a set of deterministic inclusion and exclusion rules to
456 constrain the output of local probabilistic tractography (Groot et al. 2013; Warrington et al.
457 2020). For each subject, we used the ROIs that we had drawn for the manual labeling of the
458 bundles in the other 15 subjects. We aligned the subjects to the FMRIB-58 FA template using
459 FSL's FNIRT, and then used the resulting nonlinear warp to transform the ROIs to template
460 space. We summed the corresponding ROIs of the 15 subjects, and thresholded their sum to
461 ensure that it had a size similar to that of the individual ROIs. (Empirically this was done by
462 applying a lower threshold equal to 30% of the number of subjects). The group-averaged
463 and thresholded ROIs were then mapped to the test subject using the inverse of the subject-
464 to-template registration. For each pathway, the automated multi-ROI protocol used these

465 ROIs as inclusion masks. For the bundles that were included in previously published multi-
466 ROI protocols (Warrington et al. 2020), we used the previously proposed exclusion masks
467 and augmented them as needed with the group-averaged exclusion masks from our own
468 manual dissections. Local probabilistic tractography was performed using FSL's probtrackX
469 (Behrens et al. 2007) in symmetrical mode (seeding from both inclusion masks) with default
470 parameters (5000 number of samples, 200 steps per sample, 0.5 mm step-length) and the
471 same ball-and-stick model as in the previous section (Behrens et al. 2003). We implemented
472 along-tract (PASTA) analyses for the multi-ROI approach, using the same reference
473 streamlines as for TRACULA, in the manner described in section 2.5.1 above.

474 **2.5.3 Accuracy of automated reconstruction**

475 We assessed the accuracy of the TRACULA and multi-ROI automated reconstruction by
476 comparing the tracts reconstructed automatically in the $b=1000 \text{ s/mm}^2$, 64-direction data
477 to those labeled manually in the $b_{\max}=10,000 \text{ s/mm}^2$, 512-direction data of the same subject.
478 We quantified the reconstruction error by computing the modified Hausdorff distance
479 (MHD; Dubuisson and Jain, 1994) between the automatically reconstructed and manually
480 labeled pathways. The MHD between two set of points S and T is defined as the minimum
481 distance between a point in one set and any point in the other set, averaged over all points
482 in the two sets:

$$483 \quad MHD(S, T) = \frac{1}{|S|} \sum_{s \in S} \min_{t \in T} d(s, t) + \frac{1}{|T|} \sum_{t \in T} \min_{s \in S} d(t, s)$$

484 where $d(\cdot, \cdot)$ is the Euclidean distance between a pair points from the two sets, and $|\cdot|$ is the
485 size of a set. Greater MHD indicates greater deviation of the automatically reconstructed
486 tract from the one labeled manually in the same subject, and hence lower accuracy of the
487 automated reconstruction.

488 In previous work, we reported MHD of tracts reconstructed with TRACULA using our older
489 training sets for adult brains (Yendiki et al. 2011) or infant brains (Zöllei et al. 2019), after
490 thresholding the voxel visitation maps of the automatically reconstructed tracts at a single
491 threshold (20% of the maximum, which is the default visualization threshold in TRACULA).
492 However, for the purpose of a comparison between TRACULA and the multi-ROI approach,

493 a single threshold would not be informative. The global tractography used in TRACULA adds
494 an entire end-to-end path to the voxel visitation map at each iteration, whereas the local
495 tractography used in the multi-ROI approach adds a single voxel at every iteration. As a
496 result, thresholding at the same percentage of the peak value does not yield equivalent
497 results between the two methods. For this reason, in the experiments presented here we
498 performed a more comprehensive evaluation of reconstruction error, where we increased
499 the threshold gradually from 0% to 90% for both methods, and computed their MHD at each
500 threshold.

501 In addition, for each bundle and at each threshold, we computed the true-positive rate (TPR),
502 which quantifies the proportion of the manually labeled streamlines that overlap with the
503 automatically reconstructed bundle:

$$504 \quad TPR = \left(\sum_{i=1}^N n_i \delta_i \right) / \left(\sum_{i=1}^N n_i \right),$$

505 where n_i the number of manually labeled streamlines that go through the i -th voxel, δ_i an
506 indicator function that is equal to 1 if the automatically reconstructed bundle goes through
507 the i -th voxel and 0 otherwise, and N the number of voxels in a brain volume. Each true
508 positive voxel ($\delta_i = 1$) is weighed by the number of manually labeled streamlines n_i that go
509 through that voxel, to account for the fact that the manually labeled bundles themselves
510 contain noisy tractography streamlines. Thus, a true positive should be rewarded more if it
511 occurs in a voxel that overlaps with a large number of the manually labeled streamlines.

512 In a conventional receiver operating characteristic (ROC) analysis, the TPR is plotted against
513 the false-positive rate (FPR), which quantifies the proportion of the automatically
514 reconstructed bundle that does not overlap with the manually labeled one:

$$515 \quad FPR = \left(\sum_{i=1}^N (1 - \zeta_i) \delta_i \right) / \left(\sum_{i=1}^N (1 - \zeta_i) \right),$$

516 where ζ_i an indicator function that is equal to 1 if the manually labeled bundle goes through
517 the i -th voxel and 0 otherwise. It is important to note, however, that the FPR penalizes all
518 false positive voxels equally, no matter how far away from the manually labeled bundle they
519 occur. Thus the MHD, which measures the distance between the automatically reconstructed
520 and manually labeled bundles, is a more informative metric of reconstruction errors.

521 The goal of these experiments was to investigate how close automated tractography in
522 routine-quality data could come to manually annotated tractography in high-quality data,
523 hence the “ground truth” was obtained from the manually labeled, multi-ROI tractography
524 of section 2.4. However, there were cases where even the full $b_{\max}=10,000 \text{ s/mm}^2$ data
525 yielded only a few streamlines for a certain manually labeled bundle. In those cases,
526 measuring the accuracy of the automated reconstructions by comparison to the manually
527 labeled bundle could underestimate the accuracy of the automated reconstruction. We
528 identified such cases as manually labeled bundles whose volume was less than 1/3 of the
529 median volume of the same bundle across the 16 training subjects. They were one case each
530 of the LH-CBD, LH-AR, and CC-BODY-T, and two cases of the AC. We excluded these cases
531 when computing the metrics described above, but including them would not change any of
532 our conclusions.

533 **2.5.4 Test-retest reliability of automated reconstruction**

534 We divided the 64 diffusion directions of the $b=1000 \text{ s/mm}^2$ shell into two subsets, each
535 containing 32 directions that were approximately uniformly distributed over the sphere. We
536 applied the automated reconstruction methods described in 2.5.1 and 2.5.2 to each of the
537 subsets, and we computed the accuracy metrics of 2.5.3. This allowed us to assess if the
538 results from the two methods were reproducible between the test and retest scans, and how
539 robust the methods were to even lower angular resolution.

540 **2.5.5 Test-retest reliability of along-tract measures**

541 For the bundles reconstructed from each of the two 32-direction datasets, either with
542 TRACULA or with the multi-ROI method, we extracted PASTA profiles of FA and
543 mean/radial/axial diffusivity (MD/RD/AD). We assessed the test-retest reliability of these
544 profiles by computing the symmetrized percent change (SPC) between the profiles obtained
545 by the same method from the two 32-direction datasets:

$$546 \quad SPC = \left(\sum_{i=1}^M (x_i - y_i) \right) / \left(\sum_{i=1}^M (x_i + y_i) / 2 \right),$$

547 where x_i and y_i the i -th along-tract data point of a microstructural measure
548 (FA/MD/RD/AD) from the two 32-direction datasets. The total number of data points, M ,
549 equals the number of cross-sections along a tract times the number of subjects.

550 We computed the test-retest reliability, as quantified by SPC, at a fixed level of sensitivity for
551 both reconstruction methods. For the multi-ROI method, we set the threshold for the voxel
552 visitation maps to 1% of the maximum value. At that threshold, the multi-ROI method had a
553 sensitivity of about 0.6. We then set the threshold for TRACULA (10%) to achieve the same
554 sensitivity.

555 **2.5.6 Evaluation on a larger dataset**

556 As a final evaluation, we show preliminary results from assessing the ability of TRACULA to
557 detect subtle microstructural effects in a larger dataset. We used data from 204 adolescents
558 scanned for the Boston Adolescent Neuroimaging of Depression and Anxiety (BANDA) study,
559 a Connectomes Related to Human Disease (CRHD) project. The study cohort had been
560 recruited to probe the full continuum of depressed and anxious symptoms and their co-
561 morbidity, and thus allow transdiagnostic investigations of brain-behavior relationships. It
562 included 138 participants with depression and/or anxiety disorders (age 15.50 ± 0.83 , 95
563 female) and 66 controls (age 15.17 ± 0.83 years, 36 female). Details on the clinical assessment
564 and imaging protocol are provided elsewhere (Hubbard et al. 2020; Siless et al. 2020).

565 Here we used the T1-weighted images (.8 mm isotropic resolution) to obtain structural
566 segmentations with FreeSurfer; and the lower shell of the dMRI data (1.5 mm isotropic
567 resolution, $b=1500 \text{ s/mm}^2$, 93 diffusion weighted volumes collected with two phase-encode
568 directions each, and 28 non-diffusion weighted volumes) to reconstruct WM pathways with
569 TRACULA. The dMRI data were pre-processed with FSL's *topup* (Andersson et al. 2003) and
570 *eddy* (Andersson & Sotropoulos 2016) to mitigate susceptibility and eddy-current
571 distortions. We reconstructed the following pathways with TRACULA: all subdivisions of the
572 CC, and bilateral ATR, CBD, CBV, EmC, FX, SLF1, SLF2, SLF3, UF. We studied these pathways
573 as they have been previously reported to be affected in patients with depression or anxiety
574 (Bracht et al., 2015; Greenberg et al., 2021; Henderson et al., 2013; LeWinn et al., 2014; Liao
575 et al., 2014). We tested the along-tract FA values for associations with three clinical
576 variables: the total score from the Mood and Feelings Questionnaire (MFQ; Angold et al.

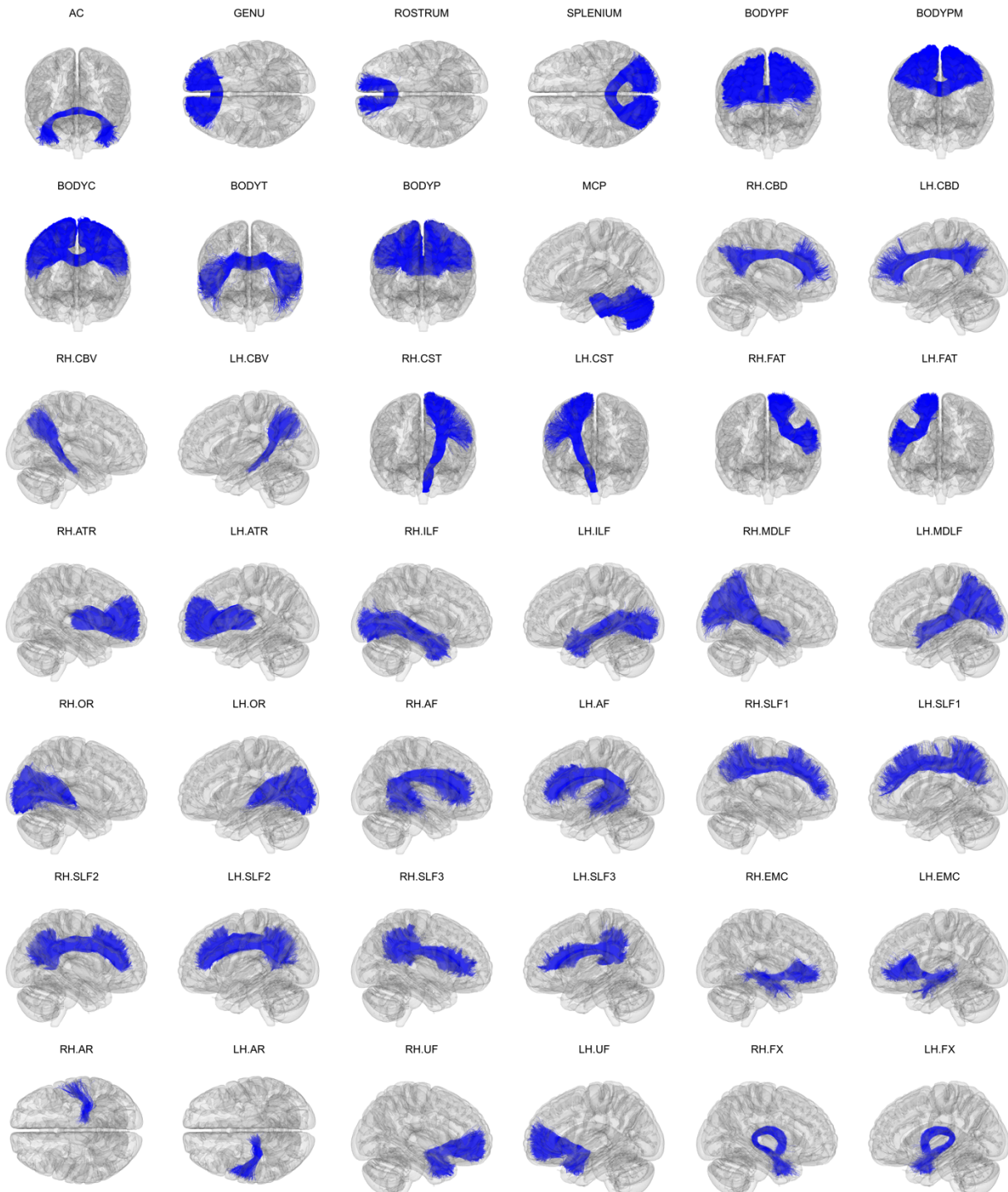
577 1995) and the depression and general anxiety subscale scores from the Revised Child
578 Anxiety and Depression Scale (RCADS; de Ross et al. 2000). We excluded two participants
579 out of the full cohort of 206 due to missing clinical scores.

580 For each clinical score, we fit a general linear model (GLM) with the along-tract FA value as
581 the dependent variable, and sex, age, and clinical score as the independent variables. We
582 tested two contrasts for statistical significance: the average slope of FA vs. clinical score, and
583 the difference of slopes between female and male participants. We used FreeSurfer statistical
584 analysis tools, adapted for 1D data; specifically, we fit a GLM at each point along each tract
585 with *mri_glmfit*, and performed simulation-based, cluster-wise correction for multiple
586 comparisons with *mri_glmfit-sim* (Hagler et al. 2006; Greve and Fischl 2018). The cluster-
587 forming threshold and the cluster-wise threshold for statistical significance were both set to
588 $p=0.05$, and 1000 simulations were performed. After statistical testing, we visualized the
589 along-tract p -values by projecting them onto a randomly selected subset of the training
590 streamlines in template space.

591 3. Results

592 3.1 Manually labeled dataset

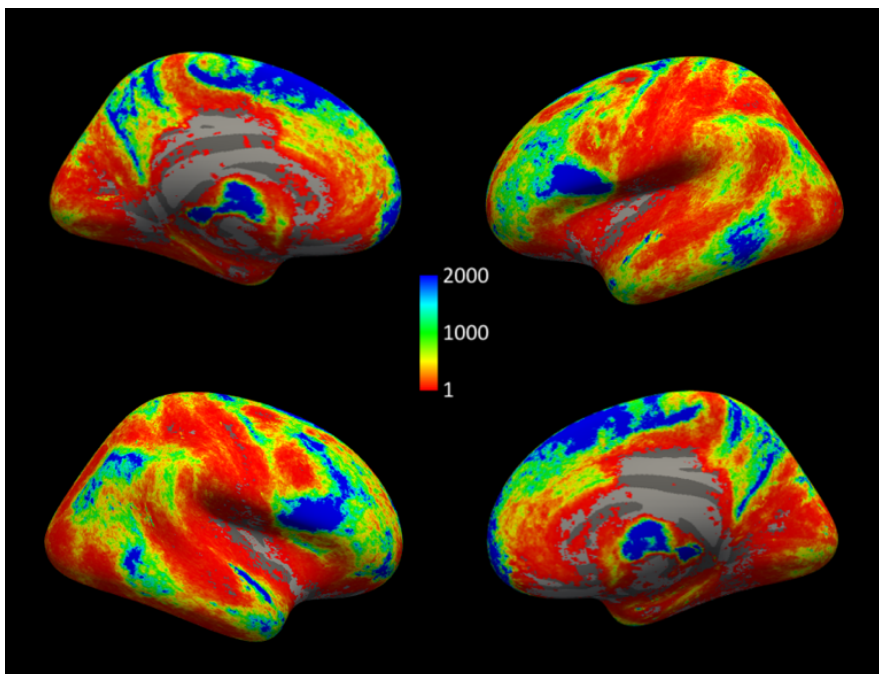
593 Fig. 5 shows the 42 manually labeled pathways. The full set includes 2.29 million annotated
594 streamlines. In individual dMRI space, they cover 82% of all cerebral and cerebellar WM
595 voxels across the 16 subjects. For Fig. 5, the streamlines were mapped to template space and
596 aggregated across all 16 training subjects. In template space, 98% of cerebral and cerebellar
597 WM voxels (defined by majority voting of the anatomical segmentations of the 16 subjects)
598 overlap with the streamlines of at least one subject. Thus, although the 42 pathways that we
599 have labeled here do not represent all brain connections, they provide extensive WM
600 coverage.



601

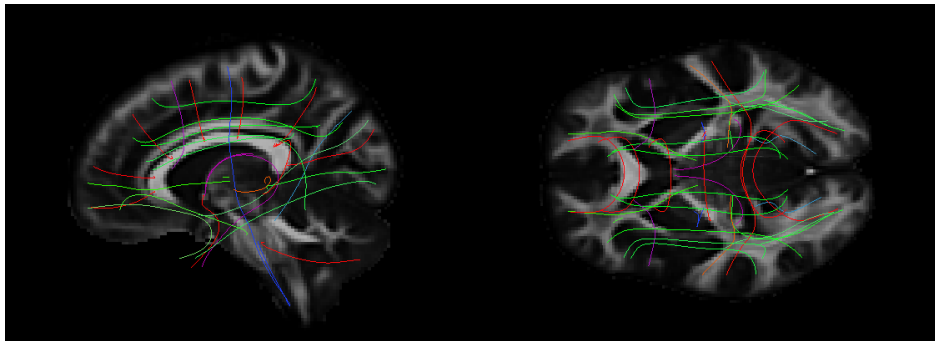
602 **Fig. 5. Manually labeled dataset.** Manually labeled streamlines from each of the 42 WM bundles are
603 shown aggregated over all 16 training subjects. Manual annotation was performed on each subject's
604 individual dMRI data as described in section 2.4. Streamlines are displayed here in 1 mm MNI-152
605 template space.

606 Fig. 6 shows the coverage of the cortical surface by the terminations of the manually labeled
607 streamlines. For this figure, the number of streamline end points per voxel were summed
608 along the normal of the surface, within 3mm from the WM-GM junction. They were then
609 mapped from each individual's surface to the *fsaverage* surface using the FreeSurfer
610 spherical morph. The total numbers of streamlines across the 16 subjects were then
611 obtained at each vertex. No smoothing was applied in the volume or on the surface to
612 produce these maps. The terminations of the manually labeled streamlines cover 89% of the
613 cortical surface on the left hemisphere and 88% on the right hemisphere.



614
615 **Fig. 6. Cortical terminations of manually labeled streamlines.** Total number of the streamlines in
616 the manually labeled set that terminate within 3 mm of each vertex on the WM-GM boundary in
617 *fsaverage* space.

618 Fig. 7 shows the FA template that we constructed from the 35 MGH-USC HCP subjects and
619 that we used as the target for inter-subject registration with ANTs. The figure also shows the
620 mean of the manually annotated streamlines from each of the 42 WM bundles. We used these
621 mean streamlines as the reference streamlines for PASTA analysis.



622

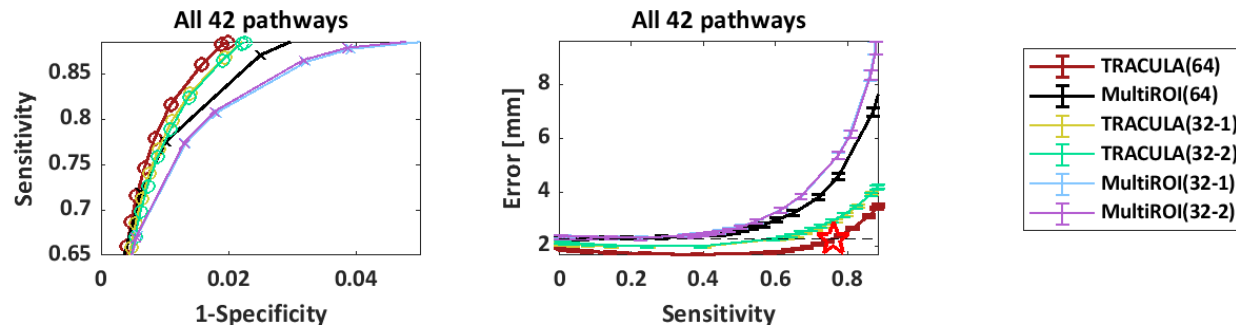
623 **Fig. 7. Template and reference streamlines.** The template that we constructed from the FA maps of
624 all 35 MGH-USC subjects is shown in sagittal (left) and axial (right) view. The mean of the manually
625 annotated streamlines from each of the 42 bundles is also shown. These serve as the reference
626 streamlines where microstructural measures are projected for PASTA analyses.

627 **3.2 Comparison of automatically reconstructed and manually labeled pathways**

628 Fig. 8 shows the accuracy measures of section 2.5.3, computed over all 42 pathways and 16
629 subjects in the leave-one-out experiments. Results are shown for the 64-direction, $b=1000$
630 s/mm^2 data with TRACULA (red) and the multi-ROI method (black); and for two sets of 32-
631 direction, $b=1000 s/mm^2$ data with TRACULA (yellow, green) and the multi-ROI method
632 (blue, purple). The plot on the left shows the sensitivity (TPR) as a function of 1-specificity
633 (FPR). The plot on the right shows the reconstruction error (MHD in mm) as a function of
634 sensitivity. Mean MHD is shown with standard error bars. Each point along the curves
635 represents a different threshold applied to the probability distributions estimated by each
636 method. The point of highest sensitivity is the one achieved by unthresholded distributions.

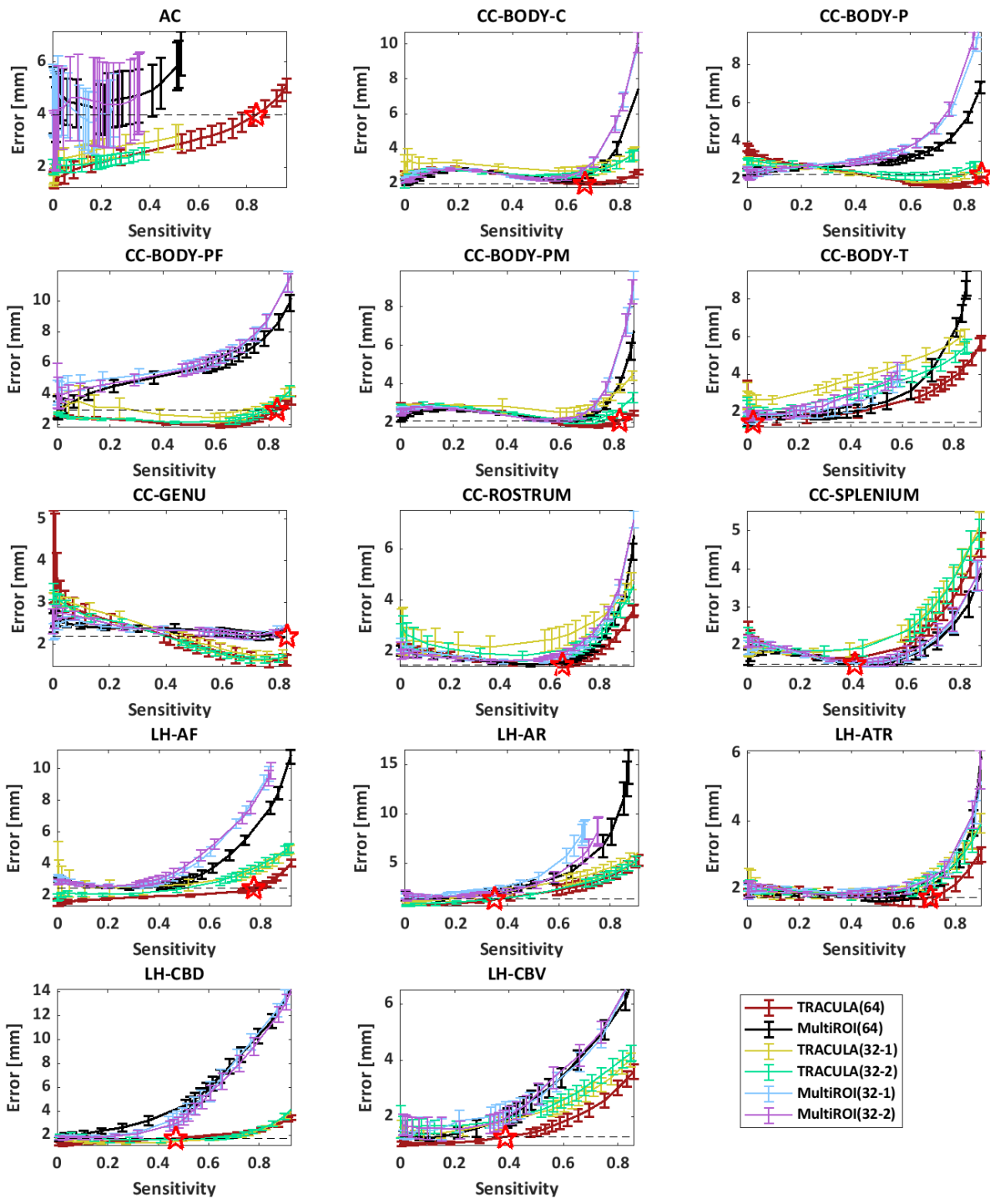
637 The highest sensitivity achieved by TRACULA across all 42 pathways was 89%, indicating
638 high coverage of the “ground-truth” pathways, *i.e.*, the ones obtained from the manual
639 labeling of the 512-direction, $b_{max}=10,000 s/mm^2$ data. At that sensitivity, the
640 reconstruction error (MHD) was 3.5 mm for TRACULA on the 64-direction data. Compared
641 to that, the reconstruction error at the same sensitivity level was 4.2 mm (20% higher) for
642 TRACULA on both sets of 32-direction data, 7.6 mm (118% higher) for the multi-ROI method
643 on the 64-direction data, and 10.6/10.4 mm (203/197% higher) for the multi-ROI method
644 on the two sets of 32-direction data. For both reconstruction methods, the overall
645 performance metrics were highly reproducible between the two sets of 32-direction data.
646 This is illustrated by the overlap of the green and yellow curves (for TRACULA) and the

647 overlap of the blue and purple curves (for the multi-ROI method). For both methods,
648 performance was somewhat lower on the 32-direction data than the 64-direction data. The
649 multi-ROI method exhibited a greater deterioration as a result of decreasing the number of
650 directions from 64 to 32.



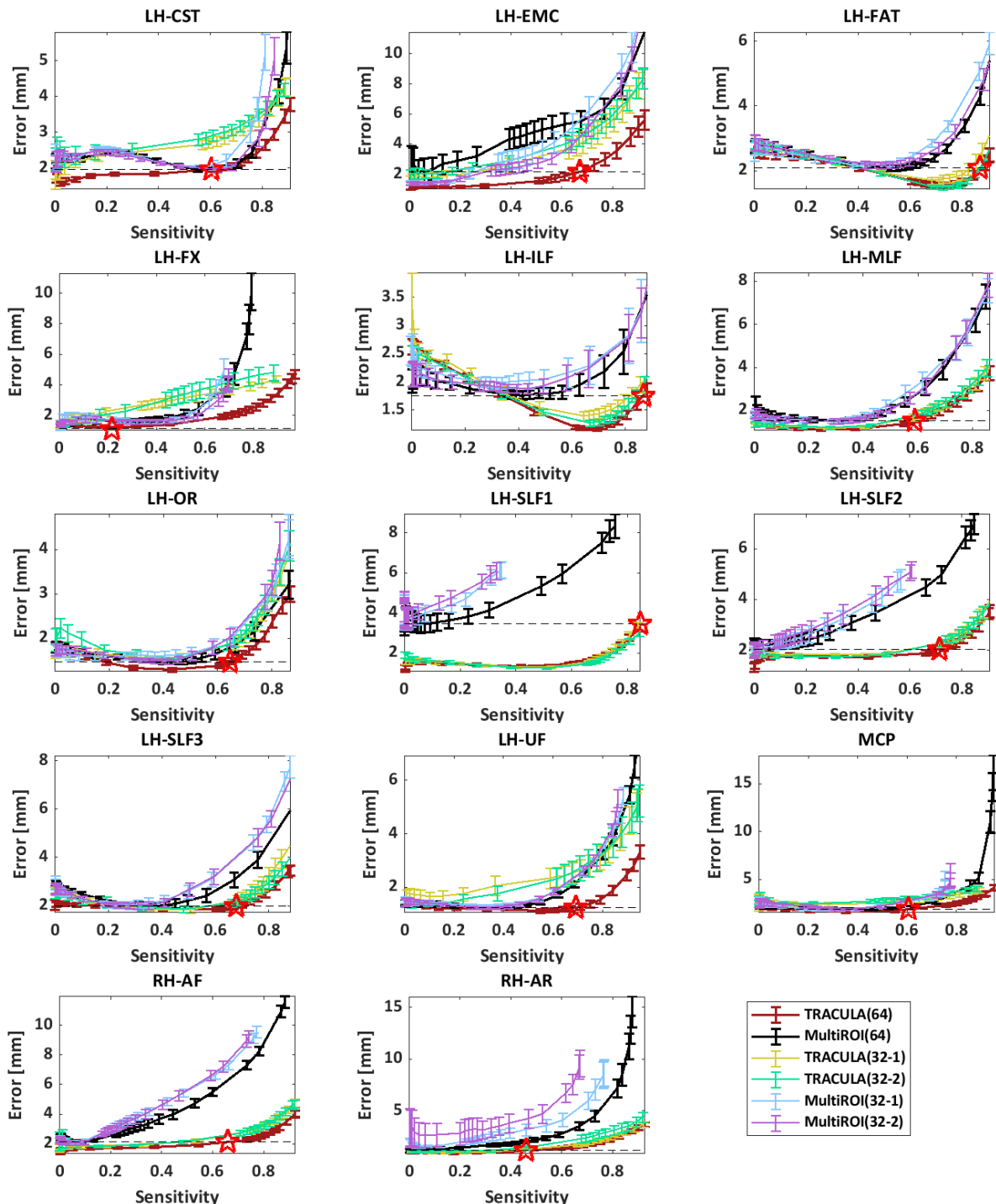
652 **Fig. 8. Overall accuracy of automated reconstruction.** For each reconstruction method (TRACULA,
653 multi-ROI), results are shown for 64 directions and for 2 sets of 32 directions. Measures were computed
654 across all 42 pathways and 16 manually labeled subjects. Each point along the curves represents a
655 different threshold applied to the estimated probability distributions. **Left:** Sensitivity (TPR) vs. 1-
656 specificity (FPR). **Right:** Reconstruction error (MHD in mm) vs. sensitivity. Horizontal dashed line:
657 minimum MHD achieved by the multi-ROI method on the 64-direction data. Red star: Maximum TPR
658 achieved by TRACULA at the same MHD level.

659 Figs. 9-11 show plots of the reconstruction error (MHD) vs. sensitivity (TPR) separately for
660 each of the 42 pathways. There was some variability across pathways in terms of the
661 difference in performance between reconstruction methods, the extent to which lowering
662 the number of directions from 64 to 32 affected their performance, or the level of
663 reproducibility between the two sets of 32 directions. However, the general patterns
664 observed from the overall performance plot of Fig. 8 could also be observed from the
665 individual pathway plots of Figs. 9-11.



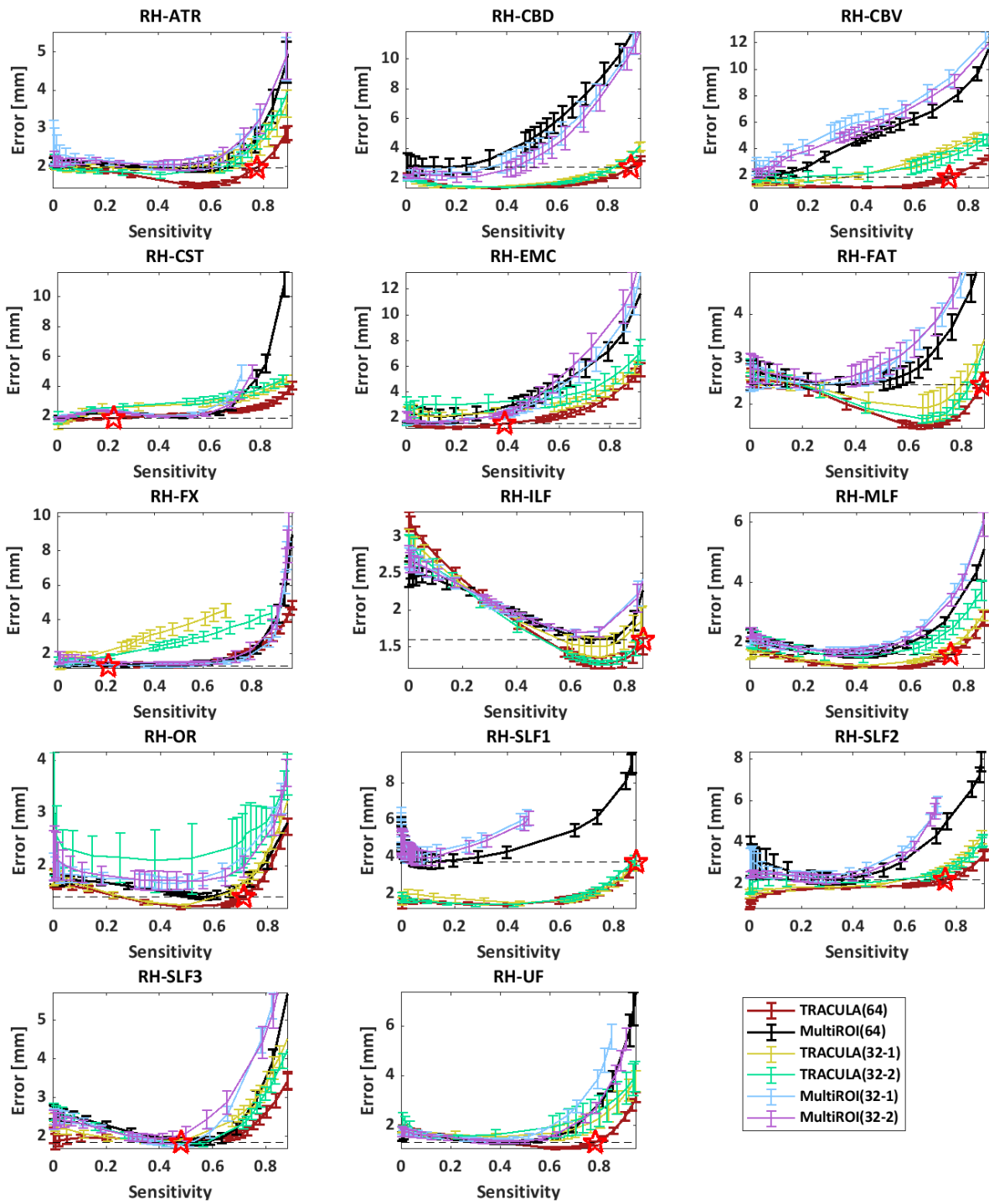
666

667 **Fig. 9. Accuracy of automated reconstruction by pathway.** For each reconstruction method
 668 (TRACULA, multi-ROI), results are shown for 64 directions and for 2 sets of 32 directions. Each point
 669 along the curves represents a different threshold applied to the estimated probability distributions. **Left:**
 670 Sensitivity (TPR) vs. 1-specificity (FPR). **Right:** Reconstruction error (MHD in mm) vs. sensitivity.
 671 Horizontal dashed line: minimum MHD achieved by the multi-ROI method on the 64-direction data. Red
 672 star: Maximum TPR achieved by TRACULA at the same MHD level.



673

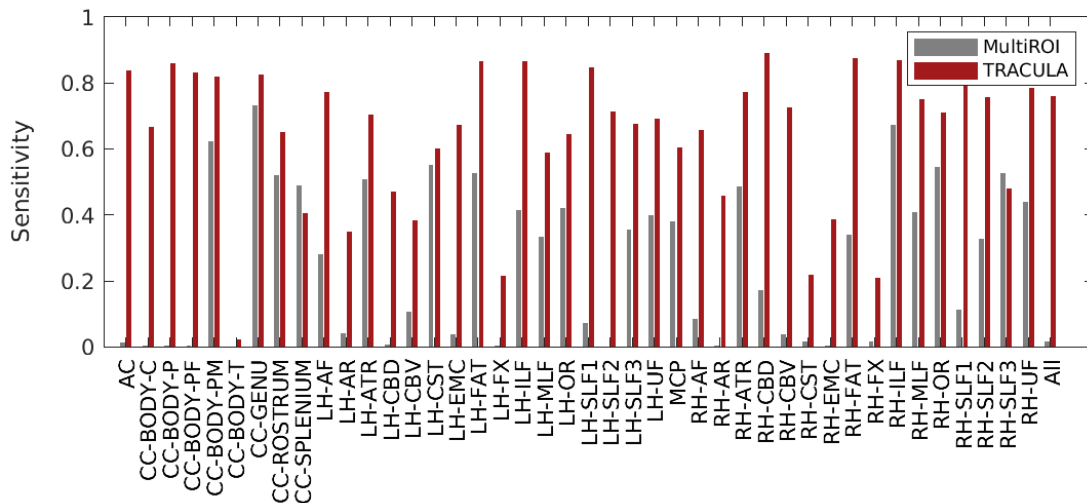
674 **Fig. 10. Accuracy of automated reconstruction by pathway (continued).** For each reconstruction
 675 method (TRACULA, multi-ROI), results are shown for 64 directions and for 2 sets of 32 directions. Each
 676 point along the curves represents a different threshold applied to the estimated probability
 677 distributions. **Left:** Sensitivity (TPR) vs. 1-specificity (FPR). **Right:** Reconstruction error (MHD in mm)
 678 vs. sensitivity. Horizontal dashed line: minimum MHD achieved by the multi-ROI method on the 64-
 679 direction data. Red star: Maximum TPR achieved by TRACULA at the same MHD level.



680

681 **Fig. 11. Accuracy of automated reconstruction by pathway (continued).** For each reconstruction
 682 method (TRACULA, multi-ROI), results are shown for 64 directions and for 2 sets of 32 directions. Each
 683 point along the curves represents a different threshold applied to the estimated probability
 684 distributions. **Left:** Sensitivity (TPR) vs. 1-specificity (FPR). **Right:** Reconstruction error (MHD in mm)
 685 vs. sensitivity. Horizontal dashed line: minimum MHD achieved by the multi-ROI method on the 64-
 686 direction data. Red star: Maximum TPR achieved by TRACULA at the same MHD level.

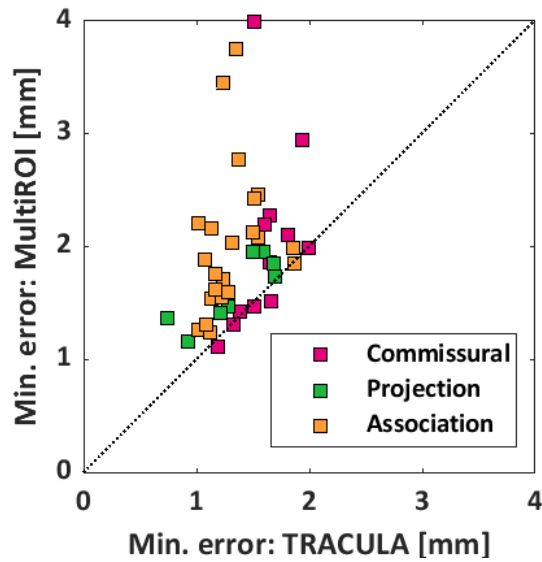
687 In the plots of reconstruction error (MHD) vs. sensitivity (TPR) from Figs. 8-11, a horizontal
688 dashed line indicates the minimum MHD that can be achieved by the multi-ROI method on
689 the 64-direction data, *i.e.*, the minimum MHD along the black curve. The portion of the red
690 curve that lies below the dashed line represents the range of operating points for which
691 TRACULA achieved a reconstruction error equal or less than the minimum achieved by the
692 multi-ROI method. The red star indicates the maximum sensitivity that TRACULA could
693 achieve while staying below that level of reconstruction error. Fig. 12 shows the sensitivity
694 (TPR) values at these operating points. The gray bars show the sensitivity of the multi-ROI
695 method at the threshold where it achieves its minimum reconstruction error. The red bars
696 show the maximum sensitivity that TRACULA could achieve while maintaining a
697 reconstruction error equal or less than the minimum error achieved by the multi-ROI
698 method (*i.e.*, the sensitivity of TRACULA at the points marked by red stars in Figs. 8-11).



699
700 **Fig. 12. Maximum sensitivity at the same level of reconstruction error.** For each of 42 pathways
701 (and across all pathways on the far right), the plot shows the sensitivity (TPR) that the multi-ROI method
702 achieves when its threshold is chosen to minimize the reconstruction error (MHD), and the maximum
703 sensitivity that TRACULA can achieve while maintaining the same or lower reconstruction error.

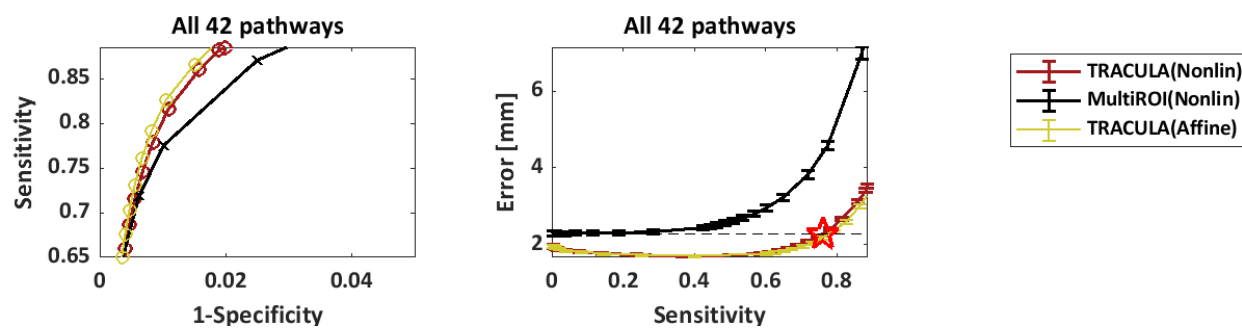
704 Fig. 13 shows the minimum reconstruction error, as quantified by the MHD in mm, achieved
705 by the multi-ROI method and TRACULA for each pathway. The x=y line is shown in black
706 dots. The data points fall mostly above the x=y line, indicating that the minimum error was
707 smaller for TRACULA than the multi-ROI method. Note that these errors do not correspond
708 to matched thresholds or matched sensitivity levels between the two methods. They are the
709 minimum errors that each method could achieve across all thresholds and thus sensitivity

710 levels. Figs. 8-11 show that, when compared at matched levels of sensitivity, TRACULA could
711 achieve overall lower reconstruction errors.



713 **Fig. 13. Minimum reconstruction error.** For each of 42 pathways, the plot shows the minimum
714 reconstruction error (MHD in mm) that can be achieved by TRACULA (x-axis) and the multi-ROI method
715 (y-axis). The pathways are color-coded based on their type (commissural, projection, or association).

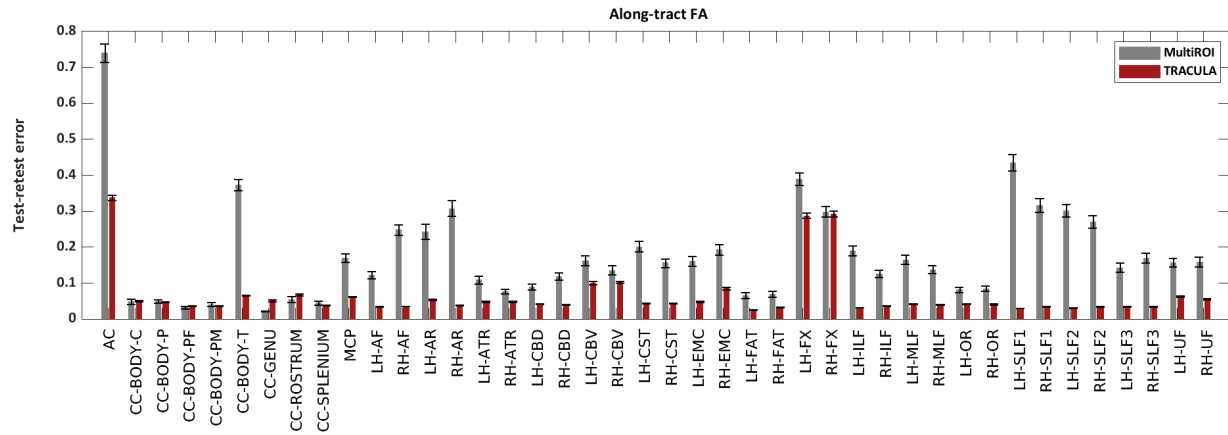
716 Fig. 14 shows that the performance of TRACULA is independent of the method that it uses
717 for inter-subject registration. The plots show results from automated reconstruction on the
718 64-direction data with three methods: TRACULA or the multi-ROI method with nonlinear
719 inter-subject registration (same as in Fig. 8), and TRACULA with affine inter-subject
720 registration. As seen in the plots, performance is indistinguishable between TRACULA with
721 the two registration approaches. This is because the anatomical priors in TRACULA do not
722 encode information about the absolute coordinates of the pathways in template space. They
723 only encode information about the relative positions (left, right, anterior, *etc.*) of the
724 pathways with respect to their surrounding anatomical structures.



726 **Fig. 14. Robustness to inter-subject registration.** Results are shown for reconstruction on the 64-
727 direction data using either TRACULA or the multi-ROI method with nonlinear inter-subject registration
728 (same as in Fig. 8), as well as TRACULA with affine inter-subject registration. Measures were computed
729 across all 42 pathways and 16 manually labeled subjects. Each point along the curves represents a
730 different threshold applied to the estimated probability distributions. **Left:** Sensitivity (TPR) vs. 1-
731 specificity (FPR). **Right:** Reconstruction error (MHD in mm) vs. sensitivity. Horizontal dashed line:
732 minimum MHD achieved by the multi-ROI method on the 64-direction data. Red star: Maximum TPR
733 achieved by TRACULA at the same MHD level.

734 **3.3 Test-retest reliability of along-tract measures**

735 Fig. 15 shows the SPC of along-tract FA values between the two 32-direction datasets, for
736 TRACULA and the multi-ROI method, at a sensitivity level of 0.6. An analysis of variance with
737 factors of bundle (42 levels) and reconstruction method (2 levels) showed a significant effect
738 of both bundle ($p=2.9\text{e-}04$) and reconstruction method ($p=3.9\text{e-}08$). Very similar results
739 were obtained for MD (bundle: $p=4.3\text{e-}03$; reconstruction method: $p=6.7\text{e-}08$), RD (bundle:
740 $p=4.3\text{e-}03$; reconstruction method: $p=5.1\text{e-}08$), and AD (bundle: $p=7.8\text{e-}03$; reconstruction
741 method: $p=5.4\text{e-}08$).



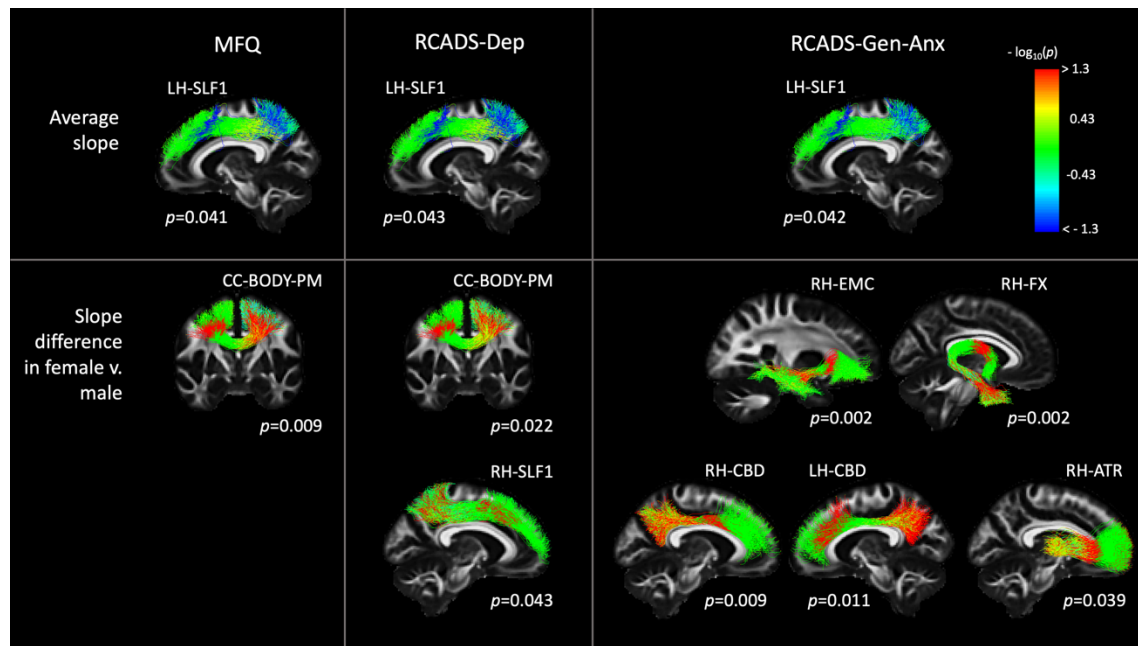
742
743 **Fig. 15. Test-retest reliability of along-tract FA.** The plots show the test-retest error of along-
744 tract (PASTA) FA values, as quantified by the SPC between along-tract FA obtained from two
745 32-direction data sets, with the multi-ROI method (gray) or with TRACULA (red). For both
746 methods, pathway probability maps were thresholded to achieve a sensitivity of 0.6.

747 These results reflect both the reliability of automated tractography and the reliability of the
748 microstructural measures themselves. For example, the two bundles where along-tract

749 FA/MD/RD/AD had their lowest reliability (AC and FX) were the ones where these tensor-
750 based measures would be the most prone to partial voluming due to proximity to CSF.
751 Microstructural measures extracted from models other the tensor may be more reliable than
752 these overall. Here, however, our main interest was in the comparison of reliability between
753 the two reconstruction methods. The median test-retest error across all 42 bundles was
754 4.3% (FA), 2.6% (MD), 5.7% (RD), 3.2% (AD) for TRACULA; and 15.7% (FA), 12.4% (MD),
755 17.0% (RD), 12.9% (AD) for the multi-ROI method.

756 **3.4 Evaluation on a larger dataset**

757 Fig. 16 shows findings from the statistical analysis of along-tract FA in the 204 subjects of
758 the BANDA cohort. The top row shows the WM bundles where the average slope of along-
759 tract FA vs. clinical score was statistically significant. We found a negative slope of FA vs.
760 clinical score in the LH-SLF1, for all three clinical scores (MFQ, RCADS-Dep, RCADS-GenAnx).
761 The bottom row shows the bundles where the difference in slopes between female and male
762 participants was statistically significant. We found greater slopes in females than males for
763 MFQ vs. FA in the CC-BODY-PM; RCADS-Dep vs. FA in the CC-BODY-PM, RH-SLF1; and
764 RCADS-GenAnx vs. FA in the RH-EMC, RH-FX, RH-CBD, LH-CBD, RH-ATR.



765
766 **Fig. 16. Associations of along-tract FA with clinical scores in the BANDA cohort.** Each column
767 shows results from a different clinical score (MFQ, RCADS-Dep, RCADS-Gen-Anx). Each row shows results
768 from a different contrast (top: average slope of FA vs. clinical score; bottom: difference in slopes of FA

769 *vs. clinical scores between female and male participants). Pathways were reconstructed automatically*
770 *with TRACULA. For display, along-tract p-values were mapped onto a randomly selected subset of the*
771 *training streamlines in template space.*

772 4. Discussion

773 In this work we present a new set of protocols for manual labeling of 42 major WM pathways
774 using probabilistic tractography on high-quality ($b_{\max}=10,000\text{ s/mm}^2$, 512-direction) dMRI
775 data from a Connectom scanner. We also demonstrate that these manually annotated
776 pathways can be used as training data to reconstruct the same pathways automatically from
777 routine-quality ($b=1000\text{ s/mm}^2$, 64-direction) dMRI data with high sensitivity and high
778 reliability.

779 4.1 Manual labeling

780 The widely used protocols for manual labeling of WM pathways were introduced at a time
781 when tractograms were typically obtained by running deterministic tensor tractography on
782 dMRI data with low b-values and low angular resolution (Wakana et al. 2007; Catani and
783 Thiebaut de Schotten 2008). These protocols were a critical step towards applying dMRI
784 tractography to population studies. They introduced the concept of the multi-ROI tract
785 dissection, which was also the first method used for automated tract-of-interest
786 reconstruction (W. Zhang et al. 2008; Clayden et al. 2009).

787 Since then, the acquisition technologies adopted and advanced by the HCP led to a dramatic
788 improvement in the quality of *in vivo* dMRI data. The higher spatial and angular resolution
789 of modern dMRI data, coupled with the use of probabilistic tractography and crossing-fiber
790 modeling techniques, yield much larger and more complex tractograms. These can be used
791 for a more detailed and accurate definition of WM pathways, but they also contain many
792 more noisy streamlines and require more clean-up. While the previously proposed manual
793 annotation protocols are an excellent starting point, they need to be updated with a greater
794 number of inclusion and exclusion ROIs. Furthermore, some pathways that were not
795 typically included in older “virtual dissection” protocols, because they could not be
796 reconstructed reliably with older data, can now be readily extracted from modern
797 tractograms.

798 In section 2.4, we presented an updated set of protocols that we deployed to label 42 WM
799 pathways manually in the MGH-USC HCP data. These data, which could only be acquired with
800 a Connectom scanner, allowed a more detailed and accurate reconstruction of major brain
801 pathways, as they had been described in anatomical studies. We were able to obtain a more
802 comprehensive delineation of the termination regions of these pathways, and to reconstruct
803 bundles or portions of bundles that were not accessible before, like the acoustic radiation
804 (Maffei et al. 2019), the more lateral terminations of the CST in the motor cortex, or the
805 Meyer loop of the OR.

806 However, our ability to reconstruct certain aspects of the more challenging WM bundles is
807 still limited, even with the best available *in vivo* dMRI data. Here we discuss some examples
808 of discrepancies between tractography on high-quality dMRI data and the anatomical
809 literature because we believe that they can be useful benchmarks for developers of
810 tractography algorithms and useful targets for future investigation with *ex vivo* dMRI. These
811 examples are from the AC, ATR, CST, FX, UF, and SLFI.

812 *AC*: The AC is a thin, long compact bundle with an uncommon C-shape that connects the two
813 temporal lobes (J. Schmahmann and Pandya 2006). In its course, the AC lies in the proximity
814 of the putamen, caudate nucleus, globus pallidus, amygdaloidal nuclei, and temporal and
815 perirhinal cortex. The vicinity to these GM structures makes the AC sensitive to partial
816 volume effects, which can severely affect its reconstruction, especially given its small size
817 (only a few voxels wide). In the temporal lobe, the AC fibers fan out towards the anterior part
818 of the temporal pole, where they merge with the fibers of the UF and FX (Cavdar et al. 2020).
819 This configuration, in which different fiber bundles merge and intermingle, is hard to resolve
820 with tractography, and it usually results in favoring the reconstruction of the bigger bundles
821 that intersect with the AC. While we could reconstruct the AC correctly in most of the 16
822 subjects, some presented only a few valid streamlines, and in most subjects the temporal
823 terminations were sparse and noisy.

824 *ATR*: We defined the ATR as cortico-thalamic fibers connecting the thalamus to the frontal
825 cortex. We recognize that this definition remains vague and reflects a tractography-based
826 characterization of this bundle more than an anatomical one (Safadi et al., 2018). Because of
827 the limitations of diffusion tractography, we are not able to precisely separate these fibers

828 from the fibers projecting from/to the brainstem, and we therefore recognize the possibility
829 that some of the latter fibers are also included in the delineation of the ATR. We also
830 observed that in all our manual dissections it was difficult to obtain the most dorsolateral
831 projections of the ATR.

832 *CST*: In our protocol, we selected only the CST projections terminating in the precentral
833 gyrus, postcentral gyri, and the posterior third of the superior frontal gyrus (SMA), as
834 described previously (Chenot et al. 2019). We are aware that the CST includes additional
835 axonal projections to more frontal regions (Dum et al., 2002). However, these were
836 represented by fewer and sparser streamlines in our tractography data, and we thus decided
837 to not include them in the present atlas. These more frontal CST projections may be harder
838 for tractography to reconstruct consistently given their bending and fanning geometry, as
839 opposed to the more straightforward CST projections to the motor regions. Future work
840 exploring specific regions of interest for tractography seeding (e.g., the subthalamic nucleus)
841 might help improve these results.

842 *FX*: The FX is a small bundle with high curvature throughout its extension. Its location in
843 proximity of the ventricles makes it sensitive to partial voluming with CSF voxels (Vos et al
844 2011). These characteristics have made this bundle extremely challenging for tractography.
845 To alleviate these limitations, we deployed a MSMT tractography algorithm (Jeurissen et al.
846 2014), which helped reduce the partial volume effect. We also avoided the use of
847 constraining binary masks (WM, GM, CSF), which reduced the number of false negatives in
848 the reconstructions. This approach allowed us to reconstruct the entire extent of the FX in
849 most of the subjects. However, despite the successful reconstruction of this bundle in most
850 subjects, a few reconstructions showed very few correct streamlines, and not all the subjects
851 presented terminations extending into the temporal regions anterior to the hippocampus.

852 *UF*: The UF has been well-characterized in tractography studies. Although tractography is
853 able to delineate the main trunk of the UF, it remains difficult to define its projections
854 precisely and to separate them from those of the EmC, given their overlap. In our protocol,
855 we aimed specifically at distinguishing these two projection systems, by including a ROI to
856 separate the medial projections of the UF from the more lateral projections of the EmC
857 (Heide et al 2013). We acknowledge the difficulty of completing this task accurately, as in

858 most subjects it led to a reduced amount of UF streamlines reaching the superior frontal
859 regions, with respect to those reaching the medial orbito-frontal regions.

860 *SLF1*: The exact human morphology of the SLF1 remains controversial, and its tractography-
861 based reconstruction challenging, with inconsistent results (Wang et al. 2016). Particularly,
862 while the literature overall agrees on its posterior terminations in the superior parietal
863 lobule and precuneus, it remains unclear whether the anterior terminations of the SLF1
864 extend anteriorly to connect regions in the SFG and possibly cingulate cortex (Howells et al.
865 2018, Thiebaut de Schotten et al. 2012, Makris et al. 2005, Kamali et al. 2014), as observed
866 in monkeys (Schmahmann et al. 2006, Thiebaut de Schotten et al. 2012), or whether they are
867 constrained to the rostral part of the supplementary motor area (SMA) and pre-SMA (Hecht
868 et al. 2015, Wassermann et al. 2013, Jang et al. 2012). This controversy arises from the fact
869 that some previously published tractography studies could not reconstruct the most anterior
870 streamlines of the SLF1 (Wassermann et al. 2013, Jang et al. 2012). While this might reflect
871 a true inter-species difference, it might also be a tractography error due to the location of
872 these fibers. They lie just underneath the u-shaped fibers of the SFG, in very close proximity
873 to the CB, and at the intersection with major inferior-superior projection systems (CST and
874 Corona Radiata) and the lateral projections of the CC. For the virtual dissection of the SLF1
875 we adopted a protocol similar to what previously described by Howell et al. 2008 and we
876 could recover the most frontal projections of the SLF1 in most of the subjects (Howells et al.
877 2018, Thiebaut de Schotten et al. 2012). However, even in these high-quality data, some
878 subjects showed only few streamlines in this most frontal region, and a few subjects showed
879 no streamlines at all. Future studies aimed at post-mortem validation of the anatomy of the
880 frontal SLF1 will help elucidate whether this is due to the anatomical configuration and
881 anatomical variability of this pathway or due to limitations of in vivo dMRI data (Maffei et al.
882 2020).

883 **4.2 Automated reconstruction**

884 We compared two ways in which our manual annotation protocol could be deployed for
885 automated tractography: *(i)* Use the manually annotated streamlines to compute the
886 anatomical neighborhood priors in TRACULA, and *(ii)* Use the manually defined ROIs as *post*
887 *hoc* constraints in a multi-ROI method. We evaluated the accuracy of bundles reconstructed
888 automatically with each approach, by comparing them to the manually annotated bundles in

889 the same subject. We found that TRACULA achieved higher sensitivity (TPR) for the same
890 reconstruction error (MHD), both overall (Fig. 8) and in individual bundles (Figs. 9-11).
891 When comparing the multi-ROI method at its lowest reconstruction error and TRACULA at
892 the same reconstruction error, the sensitivity achieved by TRACULA was an order of
893 magnitude higher (Fig. 12). Performance gains with TRACULA were similar for association,
894 commissural, and projection pathways (Fig. 13). Its performance was invariant to the inter-
895 subject registration method (Fig. 14). Finally, when compared at the same level of sensitivity,
896 the test-retest reliability of along-tract profiles extracted from microstructural measures
897 was approximately four times greater for TRACULA than the multi-ROI approach (Fig. 15).
898 These performance differences may seem surprising, especially given that TRACULA is
899 sometimes lumped together with multi-ROI methods in the literature. However, they can be
900 explained by two fundamental algorithmic differences. First, multi-ROI methods typically
901 use local tractography, which is prone to stopping or taking the wrong turn when it goes
902 through challenging areas with complex fiber configurations. The role of the ROIs in a multi-
903 ROI method is to remove these erroneous streamlines, but there is no guarantee that any
904 correct streamlines will be left. The global tractography used by TRACULA models the
905 complete trajectory of a bundle between its termination regions as a parametric curve. Thus,
906 it is not possible for the paths generated by TRACULA to stop half-way between the regions.
907 The other key algorithmic difference is in how each method incorporates prior knowledge
908 on the anatomy of the pathways of interest. Multi-ROI methods contain information about a
909 set of regions that the pathway goes through, in template space coordinates. These regions
910 are typically few (2-3), distant from each other, and deterministic. The anatomical
911 neighborhood priors used by TRACULA contain detailed probabilistic information on how
912 likely the pathway is to go through or next to each of the labels in a whole-brain anatomical
913 segmentation. This information is encoded for anatomical neighbors in multiple directions
914 and at multiple points along the pathway. These anatomical neighborhood priors implement
915 the same idea as the “Markov priors” used in the FreeSurfer automated subcortical
916 segmentation and cortical parcellation (Fischl et al. 2002; Fischl et al. 2004). The difference
917 is that TRACULA uses the anatomical neighborhood priors to generate streamlines, not to
918 classify voxels.

919 The fact that TRACULA relies on a structural segmentation from a T1-weighted scan may be
920 viewed as a limitation. However, we have previously shown that TRACULA is robust to errors
921 in the boundaries of the structural segmentation labels, or even to using a segmentation
922 mapped from a different subject (Zöllei et al. 2019). That is because TRACULA only uses
923 information on the relative position of WM pathways and structural segmentation labels
924 (e.g., how frequently is pathway A medial to structure B), and not on their exact spatial
925 coordinates. Furthermore, we have recently shown that it is possible to infer the full set of
926 FreeSurfer segmentation and parcellation labels from a dMRI scan using deep learning
927 (Ewert et al. 2020). Thus, a low-quality or missing T1-weighted scan is not an
928 insurmountable problem.

929 A possible limitation of this study is that we did not compare TRACULA to *all* possible multi-
930 ROI methods. However, we compared it to the manual annotation, which represents the best-
931 case scenario of multi-ROI performance. The manually annotated bundles were generated
932 from the $b_{\max}=10,000 \text{ s/mm}^2$ Connectom data, using state-of-the-art orientation
933 reconstruction and probabilistic tractography techniques, augmented by painstaking
934 manual editing. The bundles reconstructed automatically by TRACULA from $b=1,000 \text{ s/mm}^2$
935 data exhibited high sensitivity and low reconstruction error with respect to the manually
936 annotated bundles. In addition, we compared TRACULA to a multi-ROI method that was
937 automated and used the same input data and the same orientation reconstruction method
938 as TRACULA. In that comparison, TRACULA exhibited much higher accuracy and reliability.
939 In the future, it is possible to incorporate orientation reconstruction methods other than the
940 ball-and-stick model in TRACULA.

941 Finally, our results demonstrate that tract-of-interest reconstruction, where the task is to
942 reconstruct certain well-known, anatomically defined bundles, does not require a
943 sophisticated dMRI acquisition protocol. Our automated reconstructions from $b=1,000$
944 s/mm^2 , 64-direction data achieved an overall sensitivity of 89% with respect to the manual
945 annotations from $b_{\max}=10,000 \text{ s/mm}^2$, 512-direction data, for a reconstruction error of
946 3.5 mm for TRACULA and 4.2 mm for the multi-ROI method. Therefore, when the main use
947 of dMRI data in a study is to reconstruct tracts of interest and analyze microstructural
948 measures along them, the sophistication of the dMRI acquisition protocol should be
949 determined by the microstructural measures and not by the tractography itself.

950 **5. Conclusion**

951 We have illustrated that TRACULA can take advantage of limited-availability, high-quality
952 data that can only be acquired on a handful of Connectom scanners worldwide, to
953 reconstruct white-matter bundles with high accuracy from more modest and widely
954 available dMRI data. This allows the technological innovations of the HCP to benefit the
955 wider community that does not have access to Connectom-style scanners. Both our WM tract
956 atlas, which was annotated manually from Connectom data, and the software tools that can
957 use it to reconstruct WM bundles in routine-quality data, are freely available as part of
958 FreeSurfer 7.2.

959 **Funding:** This work was supported by the National Institute for Biomedical Imaging and
960 Bioengineering [R01-EB021265, U01-EB026996] and the National Institute for Mental
961 Health [U01-MH108168, R56-MH121426]. It was carried out at the Athinoula A. Martinos
962 Center for Biomedical Imaging at the Massachusetts General Hospital, using resources
963 provided by the Center for Functional Neuroimaging Technologies, P41-EB015896, a P41
964 Biotechnology Resource Grant supported by the National Institute of Biomedical Imaging
965 and Bioengineering (NIBIB), National Institutes of Health. The work used data acquired with
966 support from the NIH Blueprint for Neuroscience Research [U01-MH093765; part of the
967 multi-institutional Human Connectome Project, T90DA022759/R90DA023427] and relied
968 on instrumentation supported by the NIH Shared Instrumentation Grant Program
969 [S10RR023401, S10RR019307, S10RR023043].

970 **Declarations of interest:** none

971 **References**

972 Andersson J.L., Skare S., Ashburner J., 2003. How to correct susceptibility distortions in spin-
973 echo echo-planar images: application to diffusion tensor imaging. *Neuroimage*, 20(2):870-
974 88. doi: 10.1016/S1053-8119(03)00336-7.

975

976 Andersson J.L.R., Sotiropoulos S.N., 2016. An integrated approach to correction for off-
977 resonance effects and subject movement in diffusion MR imaging. *Neuroimage*,
978 15;125:1063-1078. doi: 10.1016/j.neuroimage.2015.10.019.

979 Andersson J.L.R., Graham M.S., Zsoldos E., Sotiropoulos S.N., 2016. Incorporating outlier
980 detection and replacement into a non-parametric framework for movement and distortion
981 correction of diffusion MR images. *Neuroimage*. 1;141:556-572. doi:
982 10.1016/j.neuroimage.2016.06.058.

983 Angold A., Costello E.J., Messer S.C., Pickles A., Winder F., Silver D., 1995. Development of a
984 short questionnaire for use in epidemiological studies of depression of children and
985 adolescents. *Int. J. Methods Psych. Res.*, 5:237-249.

986 Avants B.B., Epstein C.L., Grossman M., Gee J.C., 2008. Symmetric diffeomorphic image
987 registration with cross-correlation: evaluating automated labeling of elderly and
988 neurodegenerative brain. *Med Image Anal*, 12(1):26-41. doi: 10.1016/j.media.2007.06.004.

989 Avants B.B., Tustison N.J., Song G., Cook P.A., Klein A., Gee J.C., 2011. A reproducible
990 evaluation of ANTs similarity metric performance in brain image registration. *Neuroimage*,
991 54(3):2033-44. doi: 10.1016/j.neuroimage.2010.09.025.

992 Behrens T.E.J., Johansen Berg H., Jbabdi S., Rushworth M.F.S., Woolrich M.W., 2007.
993 Probabilistic diffusion tractography with multiple fibre orientations: What can we gain?
994 *NeuroImage*, 34 (1): 144-55. doi: 10.1016/j.neuroimage.2006.09.018.

995 Behrens T.E.J., Woolrich M.W., Jenkinson M., Johansen-Berg H., Nunes R.G., Clare S., Matthews
996 P.M., Brady, J.M., Smith S.M., 2003. Characterization and Propagation of Uncertainty in
997 Diffusion-Weighted MR Imaging. *Magnetic Resonance in Medicine*, 50(5): 1077-88. Doi:
998 10.1002/mrm.10609.

999 Bracht T., Linden D., Keedwell P., 2015. A review of white matter microstructure alterations
1000 of pathways of the reward circuit in depression. *Journal of Affective Disorders*, 187, 45–53.
1001 doi: 10.1016/j.jad.2015.06.041.

1002 Bürgel U., Amunts K., Hoemke L., Mohlberg H., Gilsbach J.M., Zilles K., 2006. White matter fiber
1003 tracts of the human brain: Three-dimensional mapping at microscopic resolution,
1004 topography and intersubject variability. *NeuroImage*, 29(4): 1092–1105. Doi:
1005 10.1016/j.neuroimage.2005.08.040.

1006 Calabrese E., Badea A., Coe C.L., Lubach G.R., Styner M.A., Johnson G.A., 2014. Investigating
1007 the tradeoffs between spatial resolution and diffusion sampling for brain mapping with
1008 diffusion tractography: time well spent? *Hum Brain Mapp.*, 35(11):5667-85. Doi:
1009 10.1002/hbm.22578.

1010 Catani M., Jones D.K., Ffytche D.H., 2005. Perisylvian language networks of the human brain.
1011 *Annals of Neurology*, 57(1): 8–16. doi: 10.1002/ana.20319.

1012 Catani M., Mesulam M., 2008. What is a disconnection syndrome? *Cortex* 44(8): 911–13. Doi:
1013 10.1016/j.cortex.2008.05.001.

1014 Catani M., Thiebaut de Schotten M., 2008. A diffusion tensor imaging tractography atlas for
1015 virtual in vivo dissections. *Cortex*, 44(8): 1105–32. doi: 10.1016/j.cortex.2008.05.004.

1016 Chenot, Quentin, Tzourio-Mazoyer N., Rheault F., Descoteaux M., Crivello F., Zago L., Mellet
1017 E., Jobard G., Joliot M., Mazoyer B., Petit L., 2019. A population-based atlas of the human
1018 pyramidal tract in 410 healthy participants. *Brain Structure and Function*, 224 (2): 599–612.
1019 doi: 10.1007/s00429-018-1798-7.

1020 Christiansen K., Metzler-Baddeley C., Parker G.D., Muhlert N., Jones D.K., Aggleton J.P., Vann
1021 SD., 2017. Topographic separation of fornical fibers associated with the anterior and
1022 posterior hippocampus in the human brain: An MRI-diffusion study. *Brain and Behavior*, 7
1023 (1), doi: 10.1002/brb3.604.

1024 Clayden J. D., Storkey A. J., Maniega S. M., Bastin M. E., 2009. Reproducibility of tract
1025 segmentation between sessions using an unsupervised modelling-based approach.
1026 *Neuroimage*, 45(2): 377–385. doi: 10.1016/j.neuroimage.2008.12.010.

1027 Coenen V.A., Panksepp J., Hurwitz T.A., Urbach H., Mädler B., 2012. Human Medial Forebrain
1028 Bundle (MFB) and Anterior Thalamic Radiation (ATR): Imaging of Two Major Subcortical
1029 Pathways and the Dynamic Balance of Opposite Affects in Understanding Depression. The
1030 Journal of Neuropsychiatry and Clinical Neurosciences, 24(2): 223-36. Doi:
1031 10.1176/appi.neuropsych.11080180.

1032 Dale A.M., Fischl B., Sereno M.I., 1999. Cortical Surface-Based Analysis. NeuroImage 9(2):
1033 179-94. doi: <https://doi.org/10.1006/nimg.1998.0395>.

1034 De Ross, R., Gullone, E., & Chorpita, B. (2002). The Revised Child Anxiety and Depression
1035 Scale: A Psychometric Investigation with Australian Youth. Behaviour Change, 19(2), 90-101.
1036 doi:10.1375/bech.19.2.90

1037 Desikan R.S., Ségonne F., Fischl B., Quinn B.T., Dickerson B.C., Blacker D., Buckner R.L., Dale
1038 A.M., Maguire R.P., Hyman B.T., Albert M.S., Killiany R.J., 2006. An automated labeling system
1039 for subdividing the human cerebral cortex on MRI scans into gyral based regions of interest.
1040 Neuroimage, 31(3):968-80. doi: 10.1016/j.neuroimage.2006.01.021.

1041 Dice, L.R., 1945. Measures of the Amount of Ecologic Association Between Species. Ecology
1042 26(3): 297-302. doi: 10.2307/1932409.

1043 Dick A.S., Garic D., Graziano P., Tremblay P., 2019. The frontal aslant tract (FAT) and its role
1044 in speech, language and executive function. Cortex, 111:148-163. doi:
1045 10.1016/j.cortex.2018.10.015

1046 Dubuisson M.P., Jain A.K., 1994. A modified Hausdorff distance for object
1047 matching. Proceedings of 12th International Conference on Pattern Recognition, pp. 566-
1048 568 vol.1. doi: 10.1109/ICPR.1994.576361.

1049 Dum R.P., Strick P.L., 2002. Motor areas in the frontal lobe of the primate. Physiology &
1050 Behavior, 77(4-5), 677-682. doi: 10.1016/S0031-9384(02)00929-0.

1051 Fan Q., Witzel T., Nummenmaa A., Van Dijk K.R.A., Van Horn J.D., Drews M.K., Somerville L.H.,
1052 Sheridan M.A., Santillana R.M., Snyder J., Hedden T., Shaw E.E., Hollinshead M.O., Renvall V.,
1053 Zanzonico R., Keil B., Cauley S., Polimeni J.R., Tisdall D., Buckner R.L., Wedeen V.J., Wald L.L.,
1054 Toga A.W., Rosen B.R., 2016. MGH-USC Human Connectome Project datasets with ultra-high

1055 b-value diffusion MRI. Neuroimage, 1;124(Pt B):1108-1114. doi:
1056 10.1016/j.neuroimage.2015.08.075.

1057 Fernández-Miranda J.C., Wang Y., Pathak S., Stefaneau L., Verstynen T., Yeh F.C., 2015.
1058 Asymmetry, connectivity, and segmentation of the arcuate fascicle in the human brain. Brain
1059 Structure and Function, 220(3): 1665–80. doi: 10.1007/s00429-014-0751-7.

1060 Fischl B., Sereno M.I., Dale A.M., 1999. Cortical Surface-Based Analysis. NeuroImage 9(2):
1061 195–207. doi: 10.1006/nimg.1998.0396.

1062 Fischl B., Salat D.H., Busa E., Albert M., Dieterich M., Haselgrove C., Van Der Kouwe A., Killiany,
1063 R., Kennedy D., Klaveness S., Montillo A., Makris N., Rosen B., Dale, A.M., 2002. Whole brain
1064 segmentation: Automated labeling of neuroanatomical structures in the human brain.
1065 Neuron, 33(3), 341-355. doi: 10.1016/s0896-6273(02)00569-x.

1066 Fischl B., Van Der Kouwe A., Destrieux C., Halgren E., Segonne F., Salat D.H., Busa E., Seidman
1067 L.J., Goldstein J., Kennedy D., Caviness V., Makris N., Rosen B., Dale A.M., 2004. Automatically
1068 Parcellating the Human Cerebral Cortex. Cerebral Cortex, 14(1), 11-22. doi:
1069 10.1093/cercor/bhg087.

1070 Garyfallidis E., Brett M., Correia M.M., Williams G.B., Nimmo-Smith I., 2012. QuickBundles, a
1071 Method for Tractography Simplification. Frontiers in neuroscience, 6, 175. doi:
1072 10.3389/fnins.2012.00175.

1073 Garyfallidis E., Brett M., Amirbekian B., Rokem A., van der Walt S., Descoteaux M., Nimmo-
1074 Smith I., and Dipy Contributors, 2014. Dipy, a library for the analysis of diffusion MRI data.
1075 Frontiers in Neuroinformatics, 8: 8. doi: 10.3389/fninf.2014.00008.

1076 Garyfallidis E, Côté M.A., Rheault F., Sidhu J., Hau J., Petit L., Fortin D., Cunanne S., Descoteaux
1077 M., 2018. Recognition of white matter bundles using local and global streamline-based
1078 registration and clustering. Neuroimage, 15;170:283-295. doi:
1079 10.1016/j.neuroimage.2017.07.015.

1080 Greenberg T., Bertocci M.A., Versace A., Lima Santos J. P., Chase H. W., Siffler R., Aslam H. A.,
1081 Graur S., Bebko G., Lockovich J. C., Phillips M. L., 2021. Depression and anxiety mediate the
1082 relationship between frontotemporal white matter integrity and quality of life in distressed

1083 young adults. Journal of Psychiatric Research, 132, 55–59.
1084 <https://doi.org/10.1016/j.jpsychires.2020.10.001>.

1085 Greve D.N., Fischl B., 2009. Accurate and robust brain image alignment using boundary-
1086 based registration. *NeuroImage*, 48(1): 63–72. doi: 10.1016/j.neuroimage.2009.06.060.

1087 Greve D.N., Fischl B., 2018. False positive rates in surface-based anatomical analysis.
1088 *Neuroimage*, 171:6–14. doi: 10.1016/j.neuroimage.2017.12.072.

1089 de Groot M., Vernooij M.W., Klein S., Ikram M.A., Vos F.M., Smith S.M., Niessen W.J., Andersson
1090 J.L., 2013. Improving alignment in Tract-based spatial statistics: Evaluation and optimization
1091 of image registration. *NeuroImage*, 76: 400–411. doi: 10.1016/j.neuroimage.2013.03.015.

1092 Guevara P., Poupon C., Rivi_ere, D., Cointepas Y., Descoteaux M., Thirion B., Mangin J.F., 2011.
1093 Robust clustering of massive tractography datasets. *NeuroImage*, 54(3), 1975–1993. doi:
1094 10.1016/j.neuroimage.2010.10.028.

1095 Guevara P., Duclap D., Poupon,C., Marrakchi-Kacem L., Fillard P., Le Bihan D., Leboyer M.,
1096 Houenou J., Mangin J.F., 2012. Automatic fiber bundle segmentation in massive tractography
1097 datasets using a multi-subject bundle atlas. *NeuroImage*, 61(4), 1083-1099. doi:
1098 10.1016/j.neuroimage.2012.02.071.

1099 Hagler D.J. Jr, Saygin A.P., Sereno M.I., 2006. Smoothing and cluster thresholding for cortical
1100 surface-based group analysis of fMRI data. *Neuroimage*, 33(4):1093-103. doi:
1101 10.1016/j.neuroimage.2006.07.036

1102 Hecht E.E., Gutman D.A., Bradley B.A., Preuss T.M., Stout D., 2015. Virtual dissection and
1103 comparative connectivity of the superior longitudinal fasciculus in chimpanzees and
1104 humans. *NeuroImage*, 108:124-37. doi: 10.1016/j.neuroimage.2014.12.039.

1105 Henderson S.E., Johnson A.R., Vallejo A.I., Katz L., Wong E., Gabbay V., 2013. A preliminary
1106 study of white matter in adolescent depression: Relationships with illness severity,
1107 anhedonia, and irritability. *Frontiers in Psychiatry*, 4;152. doi: 10.3389/fpsyg.2013.00152.

1108 Howells H., Thiebaut De Schotten M., Dell'acqua F., Beyh A., Zappalà G., Leslie A., Simmons A.,
1109 Murphy D.G., Catani M., 2018. Frontoparietal Tracts Linked to Lateralized Hand Preference
1110 and Manual Specialization. *Cerebral Cortex*, 1–13. doi: 10.1093/cercor/bhy040.

1111 Hubbard N.A., Siless V., Frosch I.R., Goncalves M., Lo N., Wang J., Bauer C.C.C., Conroy K., Cosby
1112 E., Hay A., Jones R., Pinaire M., Vaz De Souza F., Vergara G., Ghosh S., Henin A., Hirshfeld-
1113 Becker D.R., Hofmann S.G., Rosso I.M., Auerbach R.P., Pizzagalli D.A., Yendiki A., Gabrieli J.D.E.,
1114 Whitfield-Gabrieli S., 2020. Brain function and clinical characterization in the Boston
1115 adolescent neuroimaging of depression and anxiety study. *Neuroimage Clin.*, 27:102240. doi:
1116 10.1016/j.nicl.2020.102240.

1117 Juan Eugenio I., Insausti R., Lerma-Usabiaga G., Bocchetta M., Van Leemput K., Greve D.N., van
1118 der Kouwe A., Fischl B., Caballero-Gaudes C., Paz-Alonso P.M., 2018. A probabilistic atlas of
1119 the human thalamic nuclei combining ex vivo MRI and histology. *NeuroImage*, 183: 314–26.
1120 doi: 10.1016/j.neuroimage.2018.08.012.

1121 Juan Eugenio I., Van Leemput K., Bhatt P., Casillas C., Dutt S., Schuff N., Truran-Sacrey D.,
1122 Boxer A., Fischl B., 2015. Bayesian segmentation of brainstem structures in MRI.
1123 *NeuroImage*, 113: 184–95. doi: 10.1016/j.neuroimage.2015.02.065.

1124 Saad J., Johansen-Berg H., 2011. Tractography: Where Do We Go from Here? *Brain*
1125 *Connectivity*, 1(3): 169–83. doi: 10.1089/brain.2011.0033.

1126 Jenkinson M., Bannister P., Brady M., Smith S., 2002. Improved optimization for the robust
1127 and accurate linear registration and motion correction of brain images. *NeuroImage*, 17(2):
1128 825–41. doi: 10.1016/S1053-8119(02)91132-8.

1129 Jeurissen B., Tournier J.D., Dhollander T., Connelly A., Sijbers J., 2014. Multi-tissue
1130 constrained spherical deconvolution for improved analysis of multi-shell diffusion MRI data.
1131 *NeuroImage*, 103: 411–26. doi: 10.1016/j.neuroimage.2014.07.061.

1132 Jones D.K., Travis A.R., Eden G., Pierpaoli C., Basser P.J., 2005. PASTA: pointwise assessment
1133 of streamline tractography attributes. *Magn Reson Med.*, 53(6):1462-7. doi:
1134 10.1002/mrm.20484.

1135 Jones D.K., Knösche T.R., Turner R., 2013. White matter integrity, fiber count, and other
1136 fallacies: The do's and don'ts of diffusion MRI. *NeuroImage*, 73:239–54. doi:
1137 10.1016/j.neuroimage.2012.06.081.

1138 Kammen A., Law M, Tjan B.S., Toga A.W., Shi Y., 2016. Automated retinofugal visual pathway
1139 reconstruction with multi-shell HARDI and FOD-based analysis. *NeuroImage*, 125: 767–79.
1140 doi: 10.1016/j.neuroimage.2015.11.005.

1141 Latini F., Mårtensson J., Larsson E.M., Fredrikson M., Åhs F., Hjorthberg M., Aldskogius H.,
1142 Ryttlefors M., 2017. Segmentation of the inferior longitudinal fasciculus in the human brain:
1143 A white matter dissection and diffusion tensor tractography study. *Brain Research*, 1675:
1144 102–15. doi: 10.1016/j.brainres.2017.09.005.

1145 Lawes I.N., Barrick T.R., Murugam V., Spierings N., Evans D.R., Song M., Clark C.A., Atlas-based
1146 segmentation of white matter tracts of the human brain using diffusion tensor tractography
1147 and comparison with classical dissection. *NeuroImage*, 39(1): 62–79. doi:
1148 10.1016/j.neuroimage.2007.06.041.

1149 LeWinn K.Z., Connolly C.G., Wu J., Drahos M., Hoeft F., Ho T. C., Simmons A. N., Yang T.T., 2014.
1150 White Matter Correlates of Adolescent Depression: Structural Evidence for Frontolimbic
1151 Disconnectivity. *Journal of the American Academy of Child & Adolescent Psychiatry*, 53(8),
1152 899–909.e7. doi: 10.1016/J.JAAC.2014.04.021.

1153 Liao M., Yang F., Zhang Y., He Z., Su L., Li L., 2014. White matter abnormalities in adolescents
1154 with generalized anxiety disorder: A diffusion tensor imaging study. *BMC Psychiatry*, 14(1),
1155 1–6. doi: 10.1186/1471-244X-14-41

1156 Maffei C., Jones R., Johnson C., Wuang H., Yendiki A., 2020. Investigating SLFI anatomy using
1157 multi- resolution diffusion MRI. *ISMRM 28th Annual Meeting & Exhibition*, August 2020.

1158 Maffei C., Sarubbo S., Jovicich J., 2019. Diffusion-based tractography atlas of the human
1159 acoustic radiation. *Scientific Reports*, 9(1). doi: 10.1038/s41598-019-40666-8.

1160 Maffei C., Jovicich J., De Benedictis A., Corsini F., Barbareschi M., Chioffi F., Sarubbo S., 2018.
1161 Topography of the human acoustic radiation as revealed by ex vivo fibers micro-dissection
1162 and in vivo diffusion-based tractography. *Brain Structure and Function*, 1–11. doi:
1163 <https://doi.org/10.1007/s00429-017-1471-6>.

1164 Makris N., Papadimitriou G.M., Kaiser J.R., Sorg S., Kennedy D.N., Pandya D.N., 2009.
1165 Delineation of the middle longitudinal fascicle in humans: A quantitative, in vivo, DT-MRI
1166 study. *Cerebral Cortex*, 19(4): 777–85. doi: 10.1093/cercor/bhn124.

1167 Makris N., Kennedy D.N., McInerney S., Sorensen A.G., Wang R., Caviness V.S. Jr, Pandya D.N.,
1168 2005. Segmentation of subcomponents within the superior longitudinal fascicle in humans:
1169 a quantitative, in vivo, DT-MRI study. *Cereb Cortex*, 15(6):854-69. doi:
1170 10.1093/cercor/bhh186. Epub 2004 Dec 8. PMID: 15590909.

1171 Makris N., Preti M.G., Asami T., Pelavin P., Campbell B., Papadimitriou G.M., Kaiser J., Baselli
1172 G., Westin C.F., Shenton M.E., Kubicki M., 2013. Human middle longitudinal fascicle:
1173 variations in patterns of anatomical connections. *Brain Structure & Function*, 218(4): 951–
1174 68. doi: <https://doi.org/10.1007/s00429-012-0441-2>.

1175 Maldonado I.L., de Champfleur N.M., Velut S., Destrieux C., Zemmoura I., Duffau H., 2013.
1176 Evidence of a middle longitudinal fasciculus in the human brain from fiber dissection. *Journal
1177 of Anatomy*, 223(1): 38–45. doi: <https://doi.org/10.1111/joa.12055>.

1178 Mars R.B., Foxley S., Verhagen L., Jbabdi S., Sallet J., Noonan M.P., Neubert F.X., Andersson J.L.,
1179 Croxson P.L., Dunbar R.I., Khrapitchev A.A., Sibson N.R., Miller K.L., Rushworth M.F., 2016.
1180 The extreme capsule fiber complex in humans and macaque monkeys: a comparative
1181 diffusion MRI tractography study. *Brain Structure and Function*, 221(8): 4059–71. doi:
1182 <https://doi.org/10.1007/s00429-015-1146-0>.

1183 Menjot de Champfleur N., Lima Maldonado I., Moritz-Gasser S., Machi P., Le Bars E., Bonafé
1184 A., Duffau H., 2013. Middle longitudinal fasciculus delineation within language pathways: A
1185 diffusion tensor imaging study in human. *European Journal of Radiology*, 82(1): 151–57. doi:
1186 10.1016/j.ejrad.2012.05.034.

1187 Mori S., van Zijl P.C.M., 2002. Fiber tracking: principles and strategies - a technical review.
1188 *NMR in Biomedicine*, 15(7-8): 468–80. doi: 10.1002/nbm.781.

1189 O'Donnell L.J., Westin C.F., 2007. Automatic tractography segmentation using a high-
1190 dimensional white matter atlas. *IEEE Transactions on Medical Imaging*, 26(11), 1562-1575.
1191 doi: doi: 10.1109/TMI.2007.906785.

1192 Pascalau R., Popa Stănilă R., Sfrângăeu S., Szabo B., 2018. Anatomy of the Limbic White Matter
1193 Tracts as revealed by Fiber Dissection and Tractography. *World Neurosurgery*, 113: e672–89.
1194 doi: 10.1016/j.wneu.2018.02.121.

1195 Petrides M., Tomaiuolo F., Yeterian E.H., Pandya D.N., 2012. The prefrontal cortex:
1196 comparative architectonic organization in the human and the macaque monkey brains.
1197 *Cortex*, 48(1):46-57. doi: 10.1016/j.cortex.2011.07.002.

1198 Poletti C.E., Creswell G., 1977. Fornix system efferent projections in the squirrel monkey: An
1199 experimental degeneration study. *The Journal of Comparative Neurology*, 175(1): 101–27.
1200 doi: 10.1002/cne.901750107.

1201 Rademacher J., Bürgel U., Zilles K., 2002. Stereotaxic localization, intersubject variability, and
1202 interhemispheric differences of the human auditory thalamocortical system. *NeuroImage*,
1203 17(1): 142–60. doi: 10.1006/nimg.2002.1178.

1204 Rheault F., De Benedictis A., Daducci A., Maffei C., Tax C.M.W., Romascano D., Caverzasi E., et
1205 al. 2020. Tractostorm: The what, why, and how of tractography dissection reproducibility.
1206 *Human Brain Mapping*, 41 (7): 1859–74. doi: 10.1002/hbm.24917.

1207 Ros C., Gullmar D., Stenzel M., Mentzel H.J., Reichenbach J.R., 2013. Atlas-guided cluster
1208 analysis of large tractography datasets. *PLoS ONE*, 8(12). doi:
1209 10.1371/journal.pone.0083847.

1210 Safadi Z., Grisot G., Jbabdi S., Behrens T.E., Heilbronner S.R., McLaughlin N.C.R., Mandeville J.,
1211 Versace A., Phillips M.L., Lehman J.F., Yendiki A., Haber S.N., 2018. Functional Segmentation
1212 of the Anterior Limb of the Internal Capsule: Linking White Matter Abnormalities to Specific
1213 Connections. *J Neurosci*, 21;38(8):2106-2117. doi: 10.1523/JNEUROSCI.2335-17.2017.

1214 safaSarubbo S., De Benedictis A., Milani P., Paradiso B., Barbareschi M., Rozzanigo U.,
1215 Colarusso E., Tugnoli V., Farneti M., Granieri E., Duffau H., Chioffi F., 2015. The course and the
1216 anatomo-functional relationships of the optic radiation: a combined study with post mortem
1217 dissections and in vivo direct electrical mapping. *Journal of Anatomy*, 226(1): 47–59. doi:
1218 10.1111/joa.12254.

1219 Schmahmann, J.D., Pandya D.N., 2006. Fiber pathways of the brain. Oxford, New York: Oxford
1220 University Press.

1221 Schmahmann J.D., Pandya D.N., Wang R., Dai G., D'Arceuil H.E., De Crespigny A.J., Wedeen V.J.,
1222 2007. Association fibre pathways of the brain: Parallel observations from diffusion spectrum
1223 imaging and autoradiography. *Brain*, 130(3): 630–53. doi: 10.1093/brain/awl359.

1224 Setsompop K., Kimmlingen R., Eberlein E., Witzel T., Cohen-Adad J., McNab J.A., Keil B., Tisdall
1225 M.D., Hoecht P., Dietz P., Cauley S.F., Tountcheva V., Matschl V., Lenz V.H., Heberlein K.,
1226 Potthast A., Thein H., Van Horn J., Toga A., Schmitt F., Lehne D., Rosen B.R., Wedeen V., Wald
1227 L.L., 2013. Pushing the limits of in vivo diffusion MRI for the Human Connectome Project.
1228 *NeuroImage*, 80: 220–33. doi: 10.1016/j.neuroimage.2013.05.078.

1229 Siless V., Chang K., Fischl B., Yendiki A., 2018. AnatomicalCuts: Hierarchical clustering of
1230 tractography streamlines based on anatomical similarity. *NeuroImage*, 166:32–45. doi:
1231 10.1016/j.neuroimage.2017.10.058.

1232 Siless V., Hubbard N.A., Jones R., Wang J., Lo N., Bauer C.C.C., Goncalves M., Frosch I., Norton
1233 D., Vergara G., Conroy K., De Souza F.V., Rosso I.M., Wickham A.H., Cosby E.A., Pinaire M.,
1234 Hirshfeld-Becker D., Pizzagalli D.A., Henin A., Hofmann S.G., Auerbach R.P., Ghosh S., Gabrieli
1235 J., Whitfield-Gabrieli S., Yendiki A. 2020. Image acquisition and quality assurance in the
1236 Boston Adolescent Neuroimaging of Depression and Anxiety study. *Neuroimage Clin.*,
1237 26:102242. doi: 10.1016/j.nicl.2020.102242.

1238 Smith R.E., Tournier J.D., Calamante F., Connelly A., 2012. Anatomically-constrained
1239 tractography: Improved diffusion MRI streamlines tractography through effective use of
1240 anatomical information. *NeuroImage*, 62(3): 1924–38. doi:
1241 10.1016/j.neuroimage.2012.06.005.

1242 Tang W., Jbabdi S., Zhu Z., Cottaar M., Grisot G., Lehman J.F., Yendiki A., Haber S.N., 2019. A
1243 connectional hub in the rostral anterior cingulate cortex links areas of emotion and cognitive
1244 control. *eLife* 8:e43761. doi: 10.7554/eLife.43761.

1245 Tax C.M.W., Jeurissen B., Vos S.B., Viergever M.A., Leemans A., 2014. Recursive calibration of
1246 the fiber response function for spherical deconvolution of diffusion MRI data. *NeuroImage*
1247 86: 67–80. doi: 10.1016/j.neuroimage.2013.07.067.

1248 Thiebaut de Schotten M., Ffytche D.H., Bizzi A., Dell'Acqua F., Allin M., Walshe M., Murray R.,
1249 Williams S.C., Murphy D.G.M., Catani M., 2011. Atlasing location, asymmetry and inter-subject
1250 variability of white matter tracts in the human brain with MR diffusion tractography.
1251 *NeuroImage*, 54(1): 49–59. doi: 10.1016/j.neuroimage.2010.07.055

1252 Tournier J.D., Calamante F., Connelly, A., 2012. MRtrix: Diffusion tractography in crossing
1253 fiber regions. *Int. J. Imaging Syst. Technol.*, 22:53-66. doi: 10.1002/ima.22005

1254 Turner B.H., Mishkin M., Knapp M.E., 1979. Distribution of the anterior commissure to the
1255 amygdaloid complex in the monkey. *Brain Research*, 162(2): 331–37. doi: 10.1016/0006-
1256 8993(79)90293-2.

1257 Veraart J., Novikov D.S., Christiaens D., Ades-Aron B., Sijbers J., Fieremans E., 2016. Denoising
1258 of diffusion MRI using random matrix theory. *Neuroimage*, 15;142:394-406. doi:
1259 10.1016/j.neuroimage.2016.08.016.

1260 Visser E., Nijhuis E.H.J., Buitelaar J.K., Zwiers M.P., 2011. Partition-based mass clustering of
1261 tractography streamlines. *NeuroImage*, 54(1), 303-312. doi:
1262 10.1016/j.neuroimage.2010.07.038

1263 Vos S.B., Jones D.K., Viergever M.A., Leemans A., 2011. Partial volume effect as a hidden
1264 covariate in DTI analyses. *Neuroimage*, 15;55(4):1566-76. doi:
1265 10.1016/j.neuroimage.2011.01.048.

1266 Vos S.B., Jones D.K., Jeurissen B., Viergever M.A., Leemans A., 2012. The influence of complex
1267 white matter architecture on the mean diffusivity in diffusion tensor MRI of the human brain.
1268 *NeuroImage*, 59(3): 2208–16. doi: 10.1016/j.neuroimage.2011.09.086.

1269 Wakana S., Caprihan A., Panzenboeck M.M., Fallon J.H., Perry M., Gollub R.L., Hua K., Zhang J.,
1270 Jiang H., Dubey P., Blitz A., van Zijl P., Mori S., 2007. Reproducibility of quantitative
1271 tractography methods applied to cerebral white matter. *NeuroImage*, 36(3): 630–44. doi:
1272 10.1016/j.neuroimage.2007.02.049.

1273 Warrington S., Bryant K. L., Khrapitchev A.A., Sallet J., Charquero-Ballester M., Douaud G.,
1274 Jbabdi S., Mars R.B., Sotiropoulos S.N., 2020. XTRACT - Standardised protocols for automated
1275 tractography in the human and macaque brain. *NeuroImage*, 217:116923. doi:
1276 10.1016/j.neuroimage.2020.116923.

1277 Wassermann D., Bloy L., Kanterakis E., Verma R., Deriche R., 2010. Unsupervised white
1278 matter fiber clustering and tract probability map generation: Applications of a Gaussian
1279 process framework for white matter fibers. *NeuroImage*, 51(1), 228-241. doi:
1280 10.1016/j.neuroimage.2010.01.004.

1281 Wassermann D., Makris N., Rathi Y., Shenton M., Kikinis R., Kubicki M., Westin C.F., 2013. On
1282 describing human white matter anatomy: the white matter query language. International
1283 Conference on Medical Image Computing and Computer-Assisted Intervention (MICCAI), 16
1284 (Pt 1): 647-54.

1285 Yeatman J.D., Dougherty R.F., Myall N.J., Wandell B.A., Feldman H.M., Tract profiles of white
1286 matter properties: automating fiber-tract quantification. *PloS One* 7(11): e49790. doi:
1287 10.1371/journal.pone.0049790.

1288 Yendiki A., Panneck P., Srinivasan P., Stevens A., Zöllei L., Augustinack J., Wang R., Salat D.,
1289 Ehrlich S., Behrens T., Jbabdi S., Gollub R., Fischl B., 2011. Automated probabilistic
1290 reconstruction of white-matter pathways in health and disease using an atlas of the
1291 underlying anatomy. *Frontiers in Neuroinformatics*, 5:23. doi: 10.3389/fninf.2011.00023.

1292 Yendiki A., Reuter M., Wilkens P., Rosas H.D., Fischl B., 2016. Joint reconstruction of white-
1293 matter pathways from longitudinal diffusion MRI data with anatomical priors. *NeuroImage*,
1294 127:277-86, 2016. doi: 10.1016/j.neuroimage.2015.12.003.

1295 Zhang F., Wu Y., Norton I., Rigolo L., Rathi Y., Makris N., O'Donnell L.J., 2018. An anatomically
1296 curated fiber clustering white matter atlas for consistent white matter tract parcellation
1297 across the lifespan. *NeuroImage*, 179:429-47. doi: 10.1016/j.neuroimage.2018.06.027.

1298 Zhang W., Olivi A., Hertig S.J., van Zijl P., Mori S., 2008. Automated fiber tracking of human
1299 brain white matter using diffusion tensor imaging. *NeuroImage*, 42(2):771-77. doi:
1300 10.1016/j.neuroimage.2008.04.241.

1301 Zöllei L., Jaimes C., Saliba E., Grant P.E., Yendiki A., 2019. TRAct constrained by UnderLying
1302 INfant anatomy (TRACULInA): An automated probabilistic tractography tool with
1303 anatomical priors for use in the newborn brain. *Neuroimage*, 199:1-17. doi:
1304 10.1016/j.neuroimage.2019.05.051.